Thermodynamic Casimir effect in films: The exchange cluster algorithm

Martin Hasenbusch*
Institut für Physik, Humboldt-Universität zu Berlin, Newtonstr. 15, 12489 Berlin, Germany
(Received 31 October 2014; published 9 February 2015)

We study the thermodynamic Casimir force for films with various types of boundary conditions and the bulk universality class of the three-dimensional Ising model. To this end, we perform Monte Carlo simulations of the improved Blume-Capel model on the simple cubic lattice. In particular, we employ the exchange or geometric cluster cluster algorithm [Heringa and Blöte, Phys. Rev. E **57**, 4976 (1998)]. In a previous work, we demonstrated that this algorithm allows us to compute the thermodynamic Casimir force for the plate-sphere geometry efficiently. It turns out that also for the film geometry a substantial reduction of the statistical error can achieved. Concerning physics, we focus on (O,O) boundary conditions, where O denotes the ordinary surface transition. These are implemented by free boundary conditions on both sides of the film. Films with such boundary conditions undergo a phase transition in the universality class of the two-dimensional Ising model. We determine the inverse transition temperature for a large range of thicknesses L_0 of the film and study the scaling of this temperature with L_0. In the neighborhood of the transition, the thermodynamic Casimir force is affected by finite size effects, where finite size refers to a finite transversal extension L of the film. We demonstrate that these finite size effects can be computed by using the universal finite size scaling function of the free energy of the two-dimensional Ising model.

DOI: 10.1103/PhysRevE.91.022110 PACS number(s): 05.50.+q, 05.70.Jk, 05.10.Ln, 68.15.+e

I. INTRODUCTION

In their seminal work, de Gennes and Fisher [1] pointed out that the spatial restriction of thermal fluctuations should lead to an effective force. Due to its analogy with the Casimir effect [2], where the spatial restriction of quantum fluctuations leads to a force, it is called thermal, thermodynamic, or critical Casimir effect. Here "critical" refers to the fact that thermal fluctuations become large in the neighbourhood of a critical point. At a second order phase transition, in the thermodynamic limit of the bulk system, the correlation length, which characterizes the spatial extent of these fluctuations, behaves as

$$\xi \simeq \xi_{0,\pm} |t|^{-\nu}, \tag{1}$$

where $\xi_{0,\pm}$ are the amplitudes of the correlation length in the high and the low temperature phases, respectively, and ν is the critical exponent of the correlation length. The reduced temperature is given by $t = (T - T_c)/T_c$, where T_c is the critical temperature. Note that in the following we shall use for simplicity $t = \beta_c - \beta$, where $\beta = 1/k_B T$. For reviews on critical phenomena, see for example [3–6].

Owing to their simplicity, often films are studied. For films, the thermodynamic Casimir force per area is given by

$$F_{\text{Casimir}} = -\frac{\partial \tilde{f}_{\text{ex}}}{\partial L_0}, \tag{2}$$

where $\tilde{f}_{\text{ex}} = \tilde{f}_{\text{film}} - L_0 \tilde{f}_{\text{bulk}}$ is the excess free energy per area of the film of thickness L_0, where $\tilde{f}_{\text{film}}$ is the free energy per area of the film and $\tilde{f}_{\text{bulk}}$ is the free energy density of the bulk system. The thermodynamic Casimir force per area follows the finite size scaling law

$$F_{\text{Casimir}} \simeq k_B T L_0^{-3}\, \theta(t[L_0/\xi_{0,+}]^{1/\nu}) \tag{3}$$

(see for example Ref. [7]). The function θ is expected to be universal, which means that it should only depend on the universality classes of the transitions of the bulk system and the surfaces. For reviews on surface critical phenomena, see [8–10].

The thermodynamic Casimir effect has been demonstrated in experiments on films of ^{4}He and ^{3}He-^{4}He mixtures near the λ transition or the tricritical point of the bulk system [11–14]. The force obtained for different thicknesses is described quite well by a unique scaling function $\theta(x)$. Also, experiments with liquid binary mixtures near the mixing-demixing transition were performed, where either films [15,16] or the sphere-plate geometry [17–23] were studied. In other experiments, the thermodynamic Casimir force is the driving force for colloidal aggregation [24,25].

It is a theoretical challenge to compute the universal scaling function $\theta(x)$ for different bulk universality classes and types of boundary conditions to compare with experimental data. Still, the mean-field approximation is used as a tool that can be employed relatively easily for more complicated geometrical setups. For recent work, see for example [26,27]. Obviously, no accurate results can be expected this way. Unfortunately, field theoretic methods do not allow us to compute $\theta(x)$ for all types of boundary conditions of interest or do not allow us to compute $\theta(x)$ in the full range of the scaling variable x [28–38]. For a discussion of this point, see for example the introduction of [39]. Exact results can be obtained in the large N limit for periodic and free boundary conditions [39–46]. Also, for the two-dimensional (2D) Ising model with various boundary conditions, exact results were obtained [47–52]. In the case of the three-dimensional (3D) Ising universality class and strongly symmetry breaking boundary conditions, quite accurate results had been obtained by using the extended de Gennes–Fisher local-functional method [53–55]. O(n)-symmetric systems with periodic boundary conditions had been studied using a functional renormalization group approach [56].

*martin.hasenbusch@physik.hu-berlin.de

In the last few years, there has been considerable progress in the study of the thermodynamic Casimir force by using Monte Carlo simulations of lattice spin models. At least, in principle, the finite size scaling function can be determined with a controllable statistical and systematical error. In particular, in Refs. [57–61] the three-dimensional XY bulk universality class and a vanishing field at the boundary have been studied, which is relevant for the experiments on ^{4}He. A quite satisfactory agreement between the experimental results and the theory was found. In Refs. [26,58,59,62–72], the Ising bulk universality class and various types of boundary conditions were studied. Note that a continuous mixing-demixing transition of binary mixtures belongs to the Ising bulk universality class. Notwithstanding this nice progress, further algorithm improvements are certainly welcome to study problems with a large parameter space such as structured surfaces [26,72], disorder at the surface, the crossover from the special to the ordinary surface universality class [33], the presence of an external bulk field [69,70], or more complicated geometrical setups [27].

In Ref. [73], we determined the thermodynamic Casimir force for the plate-sphere geometry. We studied the three-dimensional Ising universality class and strongly symmetry breaking boundary conditions. A preliminary study showed that with a conventional approach and a reasonable amount of CPU time it is impossible to get meaningful results for this problem. Employing the exchange cluster algorithm, it is possible to define a variance reduced estimator for the difference of the internal energy. This allowed us to obtain the scaling functions of the thermodynamic Casimir force with high accuracy. The exchange cluster algorithm is a variant of the geometric cluster algorithm of [74]. In the geometric cluster algorithm, the sites of a single lattice are organized in pairs. This is achieved, for example, by a reflection at a plane of the lattice. The elementary operation of the update is the exchange of the spin value within such pairs of sites. Instead, we consider two independent systems. We consider pairs of sites, where one is in one lattice, while the other site belongs to the other lattice.

In this work, we apply the exchange cluster algorithm to the film geometry. The relative simplicity of the film geometry allows us to study the properties of the exchange cluster algorithm and its associated improved estimators more systematically. In this work, we first study strongly symmetry breaking boundary conditions $(+,+)$ and $(+,-)$, then $(+,O)$, and finally (O,O) boundary conditions. Here, the sign indicates the value of the spins at the boundary and O the ordinary surface transition. These problems have been studied before, and the scaling functions of the thermodynamic Casimir force are known fairly well. Here, we are mainly aiming at a better understanding of the exchange cluster algorithm before attacking more complicated problems. It turns out that, depending on the type of the surfaces of the film, large reductions of the variance can be achieved.

In the case of (O,O) boundary conditions, the problem arises that the film undergoes a second order phase transition in the universality class of the two-dimensional Ising model. This leads to sizable finite size effects, where the finite extension in the transversal directions is meant. To understand these finite size effects and the interplay of the transition with the thermodynamic Casimir force on a quantitative level, we first accurately determined the critical temperature for a large range of thicknesses L_0 by using the method discussed in Ref. [75]. We match the reduced temperature of the two-dimensional Ising model and the films. We analyze how the temperature of the effectively two-dimensional transition approaches the bulk transition temperature as the thickness of the film increases.

Based on these results, we demonstrate that finite size effects of the thermodynamic Casimir force due to the finite extension of the lattice in the transversal directions are governed by the universal finite size scaling function of the free energy density that is obtained by analyzing the two-dimensional Ising model.

The paper is organized as follows. In Sec. II, we define the model and discuss the boundary conditions that we study in this work. In Sec. IV, we discuss the exchange cluster algorithm and the variance reduced estimator for differences of the internal energy and other quantities. At the example of $(+,-)$ boundary conditions at the critical point of the bulk system, we carefully study how the performance of the algorithm depends on its parameters. In Secs. V and VI, we present our numerical results for strongly symmetry breaking and $(O,+)$ boundary conditions, respectively. In Sec. VII A, we determine the finite size scaling function of the free energy density of the two-dimensional Ising model. In Sec. VII B, we study the phase transition of films with (O,O) boundary conditions for a large range of thicknesses L_0. Then, in Sec. VII C we determine the scaling function of the thermodynamic Casimir force for films with (O,O) boundary conditions. Finally, we summarize our results and give an outlook.

II. MODEL

As in previous work, we study the Blume-Capel model on the simple cubic lattice. The bulk system, in absence of an external field, is defined by the reduced Hamiltonian

$$H = -\beta \sum_{\langle xy \rangle} s_x s_y + D \sum_x s_x^2, \tag{4}$$

where the spin might assume the values $s_x \in \{-1,0,1\}$. $x = (x_0,x_1,x_2)$ denotes a site on the simple cubic lattice, where $x_i \in \{1,2,\ldots,L_i\}$ and $\langle xy \rangle$ denotes a pair of nearest neighbors on the lattice. The inverse temperature is denoted by $\beta = 1/k_B T$. The partition function is given by $Z = \sum_{\{s\}} \exp(-H)$, where the sum runs over all spin configurations. The parameter D controls the density of vacancies $s_x = 0$. In the limit $D \to -\infty$, vacancies are completely suppressed and hence the spin-$\frac{1}{2}$ Ising model is recovered.

In $d \geqslant 2$ dimensions, the model undergoes a continuous phase transition for $-\infty \leqslant D < D_{\rm tri}$ at a β_c that depends on D, while for $D > D_{\rm tri}$ the model undergoes a first order phase transition, where $D_{\rm tri} = 2.0313(4)$ for $d = 3$ (see Ref. [76]).

Numerically, using Monte Carlo simulations it has been shown that there is a point $(D^*,\beta_c(D^*))$ on the line of second order phase transitions, where the amplitude of leading corrections to scaling vanishes. In Ref. [77], we simulated the model at $D = 0.655$ close to β_c on lattices of a linear size up to $L = 360$. We obtained $\beta_c(0.655) = 0.387\,721\,735(25)$ and $D^* = 0.656(20)$. The amplitude of leading corrections to scaling at $D = 0.655$ is at least by a factor of 30 smaller than

for the spin-$\frac{1}{2}$ Ising model. Following Eq. (12) of Ref. [68], the amplitude of the second moment correlation length in the high temperature phase at $D = 0.655$ is

$$\xi_{2\mathrm{nd},0,+} = 0.2283(1) - 1.8(\nu - 0.63002) + 275(\beta_c - 0.387\,721\,735) \quad \text{using } t = \beta_c - \beta \text{ as definition of the reduced temperature.} \tag{5}$$

In the high temperature phase, there is little difference between $\xi_{2\mathrm{nd}}$ and the exponential correlation length ξ_{exp} which is defined by the asymptotic decay of the two-point correlation function. Following [78],

$$\lim_{t \searrow 0} \frac{\xi_{\mathrm{exp}}}{\xi_{2\mathrm{nd}}} = 1.000\,200(3) \tag{6}$$

for the thermodynamic limit of the three-dimensional system. Note that in the following, ξ_0 always refers to $\xi_{2\mathrm{nd},0,+}$.

A. Film geometry and boundary conditions

In this work, we study the thermodynamic Casimir effect for systems with film geometry. In the ideal case, this means that the system has a finite thickness L_0, while in the other two directions the limit $L_1, L_2 \to \infty$ is taken. In our Monte Carlo simulations we shall study lattices with $L_0 \ll L_1, L_2$ and periodic boundary conditions in the 1 and 2 directions. Throughout, we simulate lattices with $L_1 = L_2 = L$.

The types of boundary conditions discussed here can be characterized by the reduced Hamiltonian

$$H = -\beta \sum_{\langle xy \rangle} s_x s_y + D \sum_x s_x^2 - h_1 \sum_{x, x_0 = 1} s_x - h_2 \sum_{x, x_0 = L_0} s_x, \tag{7}$$

where $h_1, h_2 \neq 0$ break the symmetry at the surfaces. In our convention, $\langle xy \rangle$ runs over all pairs of nearest neighbor sites. Note that here the sites $(1, x_1, x_2)$ and (L_0, x_1, x_2) are not nearest neighbors as it would be the case for periodic boundary conditions. In general there is ambiguity, where exactly the boundaries are located and how the thickness of the film is precisely defined. Here, we follow the convention that L_0 gives the number of layers with fluctuating spins.

First, we study strongly symmetry breaking boundary conditions that are given by $|h_1|, |h_2| \to \infty$. There are, up to symmetry transformations, two choices. Either h_1 and h_2 have the same or a different sign, which we shall denote by $(+,+)$ and $(+,-)$, respectively. Taking the limit $|h_1|, |h_2| \to \infty$ fixes the spins at the surface to the sign of the surface field.

In order to keep L_0 layers of fluctuating spins, which is done to be consistent with our previous work [63,68], we actually put the surface fields $|h_1| = |h_2| \to \infty$ at $x_0 = 0$ and $x_0 = L_0 + 1$. Note that this is equivalent to $|h_1| = |h_2| = \beta$ at $x_0 = 1$ and L_0. In a semi-infinite system, following the classification of Refs. [8–10], this choice of boundary conditions corresponds to the normal or extraordinary surface universality class.

Next, we simulated the case $h_1 = 0$ at $x_0 = 1$ and $h_2 \to \infty$ at $x_0 = L_0 + 1$. In a semi-infinite system, a vanishing external surface field corresponds to the ordinary surface universality class. Hence, we denote this combination of boundary conditions by $(O,+)$. Finally we simulated systems with $h_1 = 0$ and $h_2 = 0$ at $x_0 = 1$ and L_0. This set of boundary conditions is denoted by (O,O). In our program code we have implemented these boundary conditions by spin variables that reside at $x_0 = 0$ and $L_0 + 1$ that are fixed to either -1, 0, or 1, depending on the type of the boundary condition.

In the case of $(O,+)$ and (O,O) boundary conditions, we studied small h_1 and h_2 by computing the coefficients of the Taylor expansion of the quantities of interest up to second order around vanishing surface fields.

Given that leading bulk corrections are eliminated, the leading remaining corrections are due to the surfaces. There are theoretical arguments that these can be expressed by an effective thickness $L_{0,\mathrm{eff}} = L_0 + L_s$ of the film [79]. The value of L_s depends on the precise definition of the thickness L_0. Concerning the physics, it depends on the model that is considered and the type of boundary conditions that are imposed. However, it should be independent of the scaling variable x and the physical quantity that is considered. It can be decomposed as $L_s = l_{\mathrm{ex},1} + l_{\mathrm{ex},2}$, where $l_{\mathrm{ex},i}$ are extrapolation lengths that depend on the type of boundary conditions at the boundary i and not on the boundary conditions at the other boundary. For a discussion, see for example Sec. IV of [63] or Sec. III of [26]. In Ref. [39], the concept of an effective thickness has been verified with high numerical precision for the large N limit of the three-dimensional $O(N)$-symmetric ϕ^4 model with free boundary conditions. In the following, we shall use the numerical values $L_s = 1.91(5)$ [68] for strongly symmetry breaking boundary conditions, $L_s = 1.43(2)$ for $(O,+)$ boundary conditions [65]. In the case of (O,O) we take $L_s = 2l_{\mathrm{ex},O}$ where $l_{\mathrm{ex},O} = 0.48(1)$ [see Eq. (63) of [65]]. The estimates of L_s were obtained by analyzing the finite size scaling behavior of various quantities directly at the critical point. Analyzing the numerical results for the thermodynamic Casimir force below, we shall use these values as input.

III. COMPUTING THE THERMODYNAMIC CASIMIR FORCE

The reduced excess free energy per area of the film is defined by

$$f_{\mathrm{ex}} = -\frac{1}{L_1 L_2} \ln Z - L_0 f_{\mathrm{bulk}}, \tag{8}$$

where f_{bulk} is the reduced bulk free energy density and $Z = \sum_{\{s\}} \exp[-H(\{s\})]$ is the partition function of the film. We compute the thermodynamic Casimir force by using Eq. (2). On the lattice, the partial derivative of the reduced excess free energy per area with respect to the thickness of the film is approximated by

$$\frac{\partial f_{\mathrm{ex}}}{\partial L_0} \simeq \Delta f_{\mathrm{ex}} = \frac{f_{\mathrm{ex}}(L_0 + d/2) - f_{\mathrm{ex}}(L_0 - d/2)}{d}, \tag{9}$$

where d is a small positive integer. Except for a few preliminary algorithmic studies, we shall use the minimal value $d = 1$. Following Hucht [57], we compute the difference of free energies as integral over the inverse temperature of the difference of the corresponding internal energies

$$\Delta f_{\mathrm{ex}}(\beta) = \Delta f_{\mathrm{ex}}(\beta_0) - \int_{\beta_0}^{\beta} d\tilde{\beta}\, \Delta E_{\mathrm{ex}}(\tilde{\beta}), \tag{10}$$

where $\Delta E_{\rm ex} = \langle \Delta E \rangle - E_{\rm bulk}$ and

$$\Delta E = \frac{E(L_0 + d/2) - E(L_0 - d/2)}{d}, \tag{11}$$

where in our convention the energy per area is given by

$$E = \frac{1}{L_1 L_2} \sum_{\langle xy \rangle} s_x s_y \tag{12}$$

and $E_{\rm bulk}$ is the bulk energy density. The integration is done numerically, using the trapezoidal rule:

$$-\Delta f_{\rm ex}(\beta_n) \approx -\Delta f_{\rm ex}(\beta_0) + \sum_{i=0}^{n-1} \frac{1}{2}(\beta_{i+1} - \beta_i)[\Delta E_{\rm ex}(\beta_{i+1}) + \Delta E_{\rm ex}(\beta_i)], \tag{13}$$

where β_i are the values of β we simulated at. They are ordered such that $\beta_{i+1} > \beta_i$ for all i. Typically, $O(100)$ nodes β_i are needed to compute the thermodynamic Casimir force in the whole range of temperatures that is of interest to us. Obviously, $\Delta f_{\rm ex}(\beta_0)$ should be known with good accuracy. Usually, one chooses β_0 such that $\xi_{\rm bulk}(\beta_0) \ll L_0$ and hence $\Delta f_{\rm ex}(\beta_0) \approx 0$. In the case of strongly symmetry breaking boundary conditions, we shall use a different choice of β_0 that is discussed in Refs. [63,68].

One important aspect of this work is to demonstrate that the exchange cluster algorithm allows us to compute $\langle \Delta E \rangle$ by using a variance reduced estimator. The reduction of the variance depends on the type of the boundary conditions and the parameters L_0, d, and β as we shall see in the following. The variance of ΔE, computed in the standard way, is

$$\mathrm{var}(\Delta E) = \frac{\mathrm{var}[E(L_0 + d/2)] + \mathrm{var}[E(L_0 - d/2)]}{d^2} \approx \frac{2\,\mathrm{var}[E(L_0)]}{d^2}. \tag{14}$$

At the critical point, taking L_1 and L_2 proportional to L_0, the variance of the energy per area behaves as

$$\mathrm{var}[E(L_0)] \propto C(L_0) L_0^{-1} \propto L_0^{-1+\alpha/\nu} = L_0^{-4+2/\nu}, \tag{15}$$

where $C(L_0)$ is the specific heat of the finite system. On the other hand, the quantity we are interested in scales as

$$\Delta E_{\rm ex} \propto L_0^{-3+1/\nu} \tag{16}$$

at the critical point. Hence, the ratio

$$\frac{\mathrm{var}(\Delta E)}{(\Delta E_{\rm ex})^2} \propto \frac{L_0^2}{d^2} \tag{17}$$

which is, for a given number of statistically independent measurements, proportional to the square of the statistical error, increases with increasing thickness L_0. In order to keep the statistical error small, we used in Ref. [68] $d = 2$ and 4 for $L_0 = 33$ and 66, respectively. This in turn makes it more difficult to control the discretization error of Eq. (9). As we shall see in the following, the exchange cluster improved estimator of $\langle \Delta E \rangle$ eliminates this problem and for strongly symmetry breaking boundary conditions, we get statistically accurate results for $L_0 = 64.5$ and $d = 1$. Note that, with comparable numerical effort, $E_{\rm bulk}$ can be computed more accurately than $\langle \Delta E \rangle$, even when using the exchange cluster improved estimator. Here, we shall mainly use numerical results for $E_{\rm bulk}$ obtained in previous work [63,68]. For a discussion, see Sec. VII of [63]. Note that one could also simulate the geometry discussed in Ref. [80] by using the exchange cluster algorithm exactly in the same fashion as we simulated the sphere-plate geometry in Ref. [73]. The layer of fixed spins, called "wall" by the authors, which separates two subsystems, would take over the role of the sphere. This way the simulation allows us to measure $\Delta E_{\rm ex}$ directly. Effectively, $E_{\rm bulk}$ is provided by the larger of the two subsystems. We performed a preliminary study that demonstrated that this indeed works. However, we did not follow this line since, as discussed above, accurate results for $E_{\rm bulk}$ are already available from simulations of systems with periodic boundary conditions in all directions.

IV. EXCHANGE CLUSTER ALGORITHM

With the exchange cluster algorithm, we simulate two systems that are defined on identical lattices. Let us denote the sites of this pair of lattices by $s_{x,i}$, where x labels a site in a given lattice and $i \in \{1,2\}$ denotes the lattice. The sites of these two lattices are mapped by $T(x)$ one to one on each other such that the neighborhood relation of the sites is preserved. In the simplest case, $T(x)$ is the identity. Here, we shall use random translations along the transversal directions of the film. One also could employ reflections.

The basic operation of the exchange cluster algorithm is to exchange the values of the spins between corresponding sites. This operation can be described by an auxiliary variable $\sigma_x \in \{-1,1\}$:

$$\tilde{s}_{x,1} = \frac{1+\sigma_x}{2} s_{x,1} + \frac{1-\sigma_x}{2} s_{x,2}, \tag{18}$$

$$\tilde{s}_{x,2} = \frac{1+\sigma_x}{2} s_{x,2} + \frac{1-\sigma_x}{2} s_{x,1}. \tag{19}$$

In order to keep the notation simple, we assume $T(x) = x$. For $\sigma_x = -1$, the exchange is performed, while for $\sigma_x = 1$ the old values are kept. The contribution of a pair $\langle xy \rangle$ of nearest neighbors to the reduced Hamiltonian is given by

$$\begin{aligned} H_{\langle xy \rangle} &= -\beta(\tilde{s}_{x,1}\tilde{s}_{y,1} + \tilde{s}_{x,2}\tilde{s}_{y,2}) \\ &= -\frac{\beta}{2}(s_{x,1} - s_{x,2})(s_{y,1} - s_{y,2})\sigma_x\sigma_y \\ &\quad - \frac{\beta}{2}(s_{x,1} + s_{x,2})(s_{y,1} + s_{y,2}). \end{aligned} \tag{20}$$

Note that terms linear in σ cancel. The exchange of spins is performed by using a cluster update. The construction of the clusters is characterized by the probability to delete the link between the nearest neighbors x and y [74]:

$$p_d = \min[1, \exp(-2\beta_{\rm embed})], \tag{21}$$

where

$$\beta_{\rm embed} = \frac{\beta}{2}(s_{x,1} - s_{x,2})(s_{y,1} - s_{y,2}), \tag{22}$$

which is the prefactor of $\sigma_x\sigma_y$ in Eq. (20). This is sufficient for the problems studied in this work. Let us briefly sketch how the exchange cluster algorithm can be applied to a more general class of problems. For an enhanced coupling at the boundary, as it is required for the study of the special surface universality class, Eq. (20) has to be generalized to

$$H_{\langle xy\rangle} = -\beta_{\langle xy,1\rangle}\tilde{s}_{x,1}\tilde{s}_{y,1} - \beta_{\langle xy,2\rangle}\tilde{s}_{x,2}\tilde{s}_{y,2}. \tag{23}$$

This leads to the embedded coupling

$$\beta_{\langle xy\rangle,\mathrm{embed}} = \frac{\beta_{\langle xy,1\rangle} + \beta_{\langle xy,2\rangle}}{4}(s_{x,1} - s_{x,2})(s_{y,1} - s_{y,2}) \tag{24}$$

and in addition to an external field that acts on σ:

$$h_{x,\langle xy\rangle,\mathrm{embed}} = \frac{\beta_{\langle xy,1\rangle} - \beta_{\langle xy,2\rangle}}{4}(s_{x,1} - s_{x,2})(s_{y,1} + s_{y,2}), \tag{25}$$

where the indices of h indicate that it is the contribution to the field at the site x stemming from the pair $\langle xy\rangle$ of sites. In case there is also an external field in the original problem we get the contribution

$$h_{x,x,\mathrm{embed}} = \frac{h_{x,1} - h_{x,2}}{2}(s_{x,1} - s_{x,2}). \tag{26}$$

In total,

$$h_{x,\mathrm{embed}} = h_{x,x,\mathrm{embed}} + \sum_{y.nn.x} h_{x,\langle xy\rangle,\mathrm{embed}}. \tag{27}$$

This generalized problem can be simulated, for example, by constructing the clusters only based on the pair interaction and then taking into account the external field in the probability to flip the cluster, where here flipping a cluster means that for all sites in the cluster the spins are exchanged. For example, the cluster is flipped with the Metropolis-type probability

$$p_{\mathrm{exc},C} = \min\left[1, \exp\left(-2\sum_{x\in C} h_{x,\mathrm{embed}}\right)\right], \tag{28}$$

where the sum runs over all sites x that belong to the given cluster C.

Here, we study two films of the thicknesses $L_{0,1} = L_0 + d/2$ and $L_{0,2} = L_0 - d/2$, where $d = 1, 2, \ldots$. In the case of system 1, the spins at $x_0 = 0$ and $L_{0,1} + 1$ are fixed in order to implement the boundary conditions, while for system 2, the spins at $x_0 = 0$ and $L_{0,2} + 1$ are fixed. In order to have the same number of sites for both systems 1 and 2, we add in the case of system 2 auxiliary spins at $x_0 = L_{0,2} + 2, \ldots, L_{0,1} + 1$, which assume the same value as those at $x_0 = L_{0,2} + 1$.

Clusters are constructed according to the delete probability given by Eq. (21). This means that a link between a pair of neighbor sites is frozen with the probability $p_f = 1 - p_d$. Two sites belong to the same cluster, if there exists a chain of frozen links that connects the two sites. In order to keep the boundary conditions in place, only clusters are flipped that do not contain sites with fixed spins.

The purpose of the exchange cluster algorithm is to obtain a variance reduced estimator of $\langle \Delta E\rangle$. To this end, it is optimal to exchange as many spins as possible. Hence, only those spins are not exchanged that belong to clusters that contain fixed spins. To this end, we have to construct only those clusters that contain fixed spins. Starting the cluster at $x_0 = 0$, the cluster can not grow to $x_0 = 1$ since $s_{(0,x_1,x_2),1} = s_{(0,x_1,x_2),2}$ and hence $\beta_{\mathrm{embed}} = 0$, which implies that $p_d = 1$. Only starting from $x_0 = L_{0,2} + 1$, a cluster containing fixed spins of system 2 only, might grow to $x_0 = L_{0,2}$. Hence, we start the construction of the frozen clusters by running through all sites $x = (L_{0,2} + 1, x_1, x_2)$ and add the site $y = (L_{0,2}, x_1, x_2)$ to the frozen clusters with the probability $p_f = 1 - p_d$ [Eq. (21)]. Note that in this initial step, we have to check only this single neighbor since the other ones are frozen anyway. Then, the construction of the frozen clusters is completed using a standard algorithm for the cluster search.

In our C-program, the spins are stored in an array `char spins[I_D][L_Z][L][L];` where `I_D` equals two and `L_Z` equals $L_0 + d/2 + 2$. Similar to the case of the plate-sphere geometry, it turns out that the frozen clusters usually take only a small fraction of the lattice. Therefore, in order to save CPU time we do not copy all spins outside the frozen clusters from `spins[0][][][]` to `spins[1][][][]` and vice versa. Instead, we do that for the spins that belong to frozen clusters. This way, the systems 1 and 2 interchange their position in the array `spins`. In order to keep track of where the systems are stored in the array `spins`, we introduce the array `int posi[I_D]`, where the index `i_d` equals 1 or 2 and `posi[i_d]` indicates whether system 1 is stored in `spins[0][][][]` or `spins[1][][][]` and system 2 correspondingly. Implemented this way, the CPU time required by the cluster exchange update is essentially proportional to the size of the frozen clusters.

A. Construction of improved differences

The main purpose of the exchange cluster is to allow us to define improved estimators for the difference of observables defined in systems 1 and 2. Here, this is mainly ΔE, however, also other quantities can be computed efficiently as we shall see below. The basic idea behind these improved differences is that large parts of the configurations are swapped between the two systems. This way we get exact cancellations for most of the lattice volume. Let us consider an observable A that is defined for both systems 1 and 2. We are aiming at a variance reduced estimator for the difference

$$\Delta A = A_1 - A_2. \tag{29}$$

To this end, we make use of the correlation of the configuration of system 1 at Markov time $t + 1$ with that of system 2 at Markov time t, and vice versa:

$$\Delta A_{\mathrm{imp}} = \tfrac{1}{2}([A_{1,t} - A_{2,t+1}] + [A_{1,t+1} - A_{2,t}]), \tag{30}$$

where the second index of A now gives the position of the configuration in the Markov chain and t and $t + 1$ are separated by a single exchange cluster update.

Let us work out Eq. (30) explicitly for ΔE:

$$\begin{aligned} d\Delta E_{\rm imp} &= \frac{1}{2}\sum_{<xy>}\Big([s^{(t)}_{x,1}s^{(t)}_{y,1} - s^{(t)}_{x,2}s^{(t)}_{y,2}] + [s^{(t+1)}_{x,1}s^{(t+1)}_{y,1} - s^{(t+1)}_{x,2}s^{(t+1)}_{y,2}]\Big) \\ &= \frac{1}{2}\sum_{<xy>}\Big([s^{(t)}_{x,1}s^{(t)}_{y,1} - s^{(t+1)}_{x,2}s^{(t+1)}_{y,2}] + [s^{(t+1)}_{x,1}s^{(t+1)}_{y,1} - s^{(t)}_{x,2}s^{(t)}_{y,2}]\Big) \\ &= \frac{1}{2}\sum_{<xy>\in C_f}\Big([s^{(t)}_{x,1}s^{(t)}_{y,1} - s^{(t+1)}_{x,2}s^{(t+1)}_{y,2}] + [s^{(t+1)}_{x,1}s^{(t+1)}_{y,1} - s^{(t)}_{x,2}s^{(t)}_{y,2}]\Big), \end{aligned} \tag{31}$$

where $\langle xy\rangle \in C_f$ means that at least one of the sites x or y belongs to a frozen cluster. Hence, also the numerical effort to compute $\Delta E_{\rm imp}$ is approximately proportional to the size of the frozen clusters. Note that for our choice of the update

$$s^{(t+1)}_{x,1}s^{(t+1)}_{y,1} = s^{(t)}_{x,2}s^{(t)}_{y,2} \quad \text{and} \quad s^{(t+1)}_{x,2}s^{(t+1)}_{y,2} = s^{(t)}_{x,1}s^{(t)}_{y,1} \tag{32}$$

for all nearest neighbor pairs $\langle x,y\rangle$ where neither x nor y belongs to a frozen cluster.

B. The simulation algorithm, benchmarks, and tuning of parameters

The exchange cluster algorithm on its own is not ergodic since it keeps the total number of spins of a given value fixed. Therefore, we performed in addition updates of the individual systems, using standard cluster and local updates [81]. In all our simulations, we used the SIMD-oriented fast Mersenne twister algorithm [82] as pseudorandom number generator.

1. *Cluster algorithm for the individual system*

We used the standard delete probability $p_d = \min[1, \exp(-2\beta s_x s_y)]$ in the construction of the clusters. One has to take into account that clusters that contain sites with fixed spins can not be flipped. Flipped means that all spins that belong to the cluster are multiplied by -1. We have used two types of cluster updates. In the first one, denoted by SW-cluster algorithm in the following, we flip the clusters that do not contain fixed sites, following Ref. [83], with the probability $\frac{1}{2}$. In the second one, denoted by B-cluster algorithm in the following, clusters that do not contain fixed sites are always flipped. This has the technical advantage that actually only clusters that contain sites with fixed spins have to be constructed. All other spins are flipped. For (O,O) boundary conditions, only the SW-cluster algorithm is used since for $s_x = 0$ or $s_y = 0$ we get $p_d = 1$ and hence there are no clusters that contain both sites of the interior and the boundary.

2. *Todo-Suwa algorithm*

The authors of [84] have pointed out that autocorrelation times of local updating algorithms can be reduced by a significant factor, when one abstains from detailed balance and only demands the sufficient condition of balance. This idea still leaves considerable freedom for the design of the algorithm. Todo and Suwa suggest to order the possible values of the local spin on a cycle. Then, one preferentially updates in one of the two directions on the cycle. For the precise description, see Ref. [84]. Todo and Suwa have tested their algorithm for example at the four- and eight-state Potts models in two dimensions in the neighborhood of the critical point. They find a reduction of the autocorrelation time compared with the heat-bath algorithm by a factor of 2.7 and 2.6 for the four- and eight-state Potts model, respectively. In the case of the improved Blume-Capel model on the simple cubic lattice at the critical point one finds a reduction by a factor of about 1.7 compared with the heat-bath algorithm [85]. Since we failed to find a prove of ergodicity for the Todo-Suwa local update, sweeping through the lattice in typewriter fashion, we performed heat-bath sweeps in addition. Note that for the heat bath the proof of ergodicity is trivial.

3. *Update cycle*

We initialized the spins that are not fixed by choosing one of the three possible values with equal probability. Then, we equilibrated the systems by performing 1000 update cycles consisting of one heat-bath sweep, one SW-cluster update, one Todo-Suwa sweep, and one B-cluster update. In the case of (O,O) boundary conditions, the B-cluster update is omitted.

After this initial phase of the simulation we added $n_{\rm exc}$ exchange cluster updates to each update cycle. Furthermore, since the frozen exchange clusters are very much localized at the boundary, we performed for each exchange cluster update a local update with the Todo-Suwa algorithm of the i_r layers of the lattices that are closest to the upper boundary. Only in a few preliminary tests we shall use a different sequence of updates, which will be stated in the following.

4. *Tuning the parameters of the update cycle and benchmarking the algorithm*

First, we tested the performance of the exchange cluster algorithm for $(+,-)$ boundary conditions at the critical point $\beta_c = 0.387\,721\,735$. To keep things simple, we first used the following update sequence: A global sweep with the heat-bath algorithm over both systems followed by one exchange cluster update, combined with a random translation of one system with respect to the other in the transversal directions. Our results are summarized in Table I. In all cases, 10^5 update cycles and measurements were performed. In the third column, we give the size of the frozen exchange clusters per area S_c. The $d = L_{0,1} - L_{0,2}$ layers, where the spins of system 2 are fixed and those of system 1 are not, are taken into account in S_c. This means that S_c at least equals to d. We find that S_c is small compared with the thickness of the films in all cases. For given d it depends very little on the thickness L_0. As one might

TABLE I. We study the properties of the exchange cluster algorithm for $(+,-)$ boundary conditions at β_c. The transversal extension of the lattices is $L = 32$, 64, and 128 for $L_{0,2} = 8$, 16, and 32, respectively. For the definition of the quantities and a discussion, see the text.

$L_{0,1}$	$L_{0,2}$	S_c	$\mathrm{var}(d\Delta E_{\mathrm{imp}})/L^2$	$\tau_{\mathrm{int,imp}}$	$[\mathrm{var}(E_1)+\mathrm{var}(E_2)]/L^2$	τ_{int,E_1}	τ_{int,E_2}
9	8	1.4462(11)	35.5(2)	1.21(2)	144.2(6)	1.67(3)	1.37(3)
17	16	1.4538(12)	58.4(3)	1.40(4)	378.(2.)	2.97(10)	2.62(9)
18	16	2.7966(21)	96.3(6)	2.28(7)	399.(2.)	3.61(13)	2.85(10)
33	32	1.4547(11)	89.8(5)	1.52(6)	995.(6.)	9.6(7)	9.2(6)
34	32	2.8001(22)	152.4(10)	2.67(11)	982.(6.)	9.6(7)	7.5(5)
36	32	5.3388(41)	252.(2.)	5.70(33)	1046.(7.)	9.6(7)	8.3(6)

expect, it increases with increasing d. We give the variance of $d\Delta E_{\mathrm{imp}}$ and of the energies E_1 and E_2 normalized by the area L^2 since this normalized number should have a finite $L \to \infty$ limit. We find that the variance of $d\Delta E_{\mathrm{imp}}$ is reduced compared with the sum of the variances of the energies E_1 and E_2 of the individual systems. For fixed d, the ratio of the two variances increases with increasing lattice size. On the other hand, the advantage of the improved estimator becomes smaller with increasing d. Often, variance reduced estimators have a larger integrated autocorrelation time than the basic quantity. Here, in contrast we observe that the integrated autocorrelation time of ΔE_{imp} is considerably smaller than those of the energies E_1 and E_2 of the individual systems.

Next, we studied an update cycle that includes cluster updates of the individual films. In particular, we used the update cycle stated in Sec. IV B 3 above: one sweep with the heat-bath algorithm, a SW-cluster update, one sweep with the Todo-Suwa algorithm, and a B-cluster update.

Motivated by the fact that S_c is small and hence the CPU time required by the exchange cluster update is little and that the integrated autocorrelation time $\tau_{\mathrm{int,imp}}$ is relatively small, we performed n_{exc} exchange cluster updates for each update cycle. Furthermore, since the frozen exchange clusters are very much localized at the upper boundary, a sweep with the local Todo-Suwa algorithm of the i_r layers that are closest to the upper boundary is performed. In the following, we try to find the optimal choice for the parameters n_{exc} and i_r. Again, we perform this study at the critical point for $(+,-)$ boundary conditions.

As an example, let us consider the pair of lattices characterized by $d = 1$, $L_0 = 32.5$, and $L = 128$. On our CPU, the time required by a single exchange cluster update is about 0.014 times the one needed for the total of the SW-cluster, B-cluster updates, and the heat-bath and Todo-Suwa sweeps. Updating one layer in both lattices using the Todo-Suwa algorithm takes about 0.0049 times the CPU time of these updates. Hence, the CPU time required by the complete cycle is proportional to

$$t_{\mathrm{mix}} = 1 + n_{\mathrm{exc}}(0.014 + 0.0049 i_r). \tag{33}$$

We define a performance index as

$$I_{\mathrm{perf}} = \frac{\mathrm{var}[E_1 - E_2]\ \tau_{\mathrm{int},E_1-E_2}}{t_{\mathrm{mix}}\ \mathrm{var}[d\Delta E_{\mathrm{imp}}]\ \tau_{\mathrm{int,imp}}}, \tag{34}$$

where $\mathrm{var}[E_1 - E_2]$ and $\tau_{\mathrm{int},E_1-E_2}$ are taken from a simulation with $n_{\mathrm{exc}} = 0$, i.e., without any exchange cluster update. We simulated for a large number of values of n_{exc} and i_r. The number of update cycles ranges from 2×10^5 to 10^6. Our results are plotted in Fig. 1. Among our choices, the optimal performance is reached for $i_r = 4$ and $n_{\mathrm{exc}} = 32$. For these parameters, the improvement is $I_{\mathrm{perf}} = 152.0(1.3)$, which means that the improved cluster exchange estimator allows us to reduce the statistical error by more than a factor of 12 at a given CPU time. We also see that this maximum is rather shallow, which means that no accurate fine tuning of the algorithm is needed to reach a fair fraction of the optimum.

We performed an analogous study for $L_0 = 16.5$ and 64.5, simulating a smaller number of values of i_r and n_{exc}, focusing on finding the optimal values. For $L_0 = 16.5$, the maximum is also reached for $i_r = 4$ and $n_{\mathrm{exc}} = 32$ with $I_{\mathrm{perf}} = 45.5(3)$. Also, here the maximum of I_{perf} is very shallow. For example, for $i_r = 4$ and $n_{\mathrm{exc}} = 16$ we get $I_{\mathrm{perf}} = 40.3(3)$ or for $i_r = 2$ and $n_{\mathrm{exc}} = 32$ we get $I_{\mathrm{perf}} = 43.0(3)$. For $L_0 = 64.5$, the optimum is located at $i_r = 8$ and $n_{\mathrm{exc}} = 64$ with $I_{\mathrm{perf}} = 553.(13.)$. For $i_r = 4$ and $n_{\mathrm{exc}} = 32$ we get $I_{\mathrm{perf}} = 505.(10.)$. For $d = 1$ fixed, I_{perf} increases almost like L_0^2 with increasing thickness. This means that the problem of the increasing variance [Eq. (17)] of the standard estimator is cured by the improved estimator.

Here, we performed a random translation of the systems with respect to each other in the lateral directions performing the cluster exchange update. Studying, for example, random

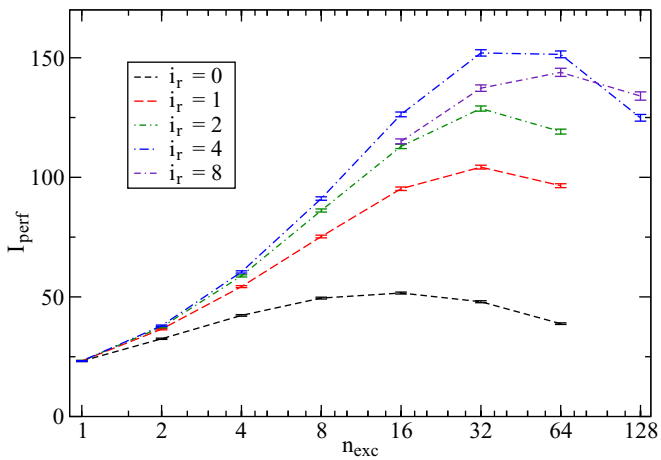

FIG. 1. (Color online) We study $(+,-)$ boundary conditions at the critical point. We simulated a pair of lattices characterized by $L_0 = 32.5$, $d = 1$, and $L = 128$. We plot the performance index I_{perf} defined in Eq. (34) as a function of the number n_{exc} of exchange cluster updates per update cycle. Results are given for $i_r = 0$, 1, 2, 4, and 8. For a discussion, see the text.

disorder at the boundary, this symmetry is not available. Therefore, we checked how much the performance gain $I_{\rm perf}$ depends on these translations. To this end, we repeated the simulations for $L_0 = 32.5$, $i_r = 4$, and $n_{\rm exc} = 32$ without these translations. It turns out that $I_{\rm perf}$ is smaller by a factor of about 1.6. This means that one certainly should use the translation when the symmetry is present. However, the effectiveness of the cluster exchange update does not crucially depend on it.

Likely further improvements can be achieved by exploiting, for example, reflection symmetries. Also, a more elaborate update cycle might improve the performance. We did not further explore these ideas. Actually, we did not systematically tune the parameters i_r and $n_{\rm exc}$ for the whole range of temperatures and different boundary conditions discussed below. Throughout, we used $n_{\rm exc} = 20$. In fact, we had started our simulations before performing the systematic tuning discussed above.

V. THERMODYNAMIC CASIMIR FORCE FOR STRONGLY SYMMETRY BREAKING BOUNDARY CONDITIONS

These boundary conditions have been studied by using Monte Carlo simulations of the Ising model [58,59,66,68] and the improved Blume-Capel model [63,68] before. Here, we simulated films of the thicknesses $L_0 = 16.5$, 32.5, and 64.5. Throughout, we use $d = 1$. In the case of $(+,+)$ boundary conditions the correlation length of the film stays small, it reaches a maximum at $x = t[L_{0,\rm eff}/\xi_0]^{1/\nu} \approx 7$, where $\xi_{\rm 2nd,film} \approx 0.145 L_{0,\rm eff}$ (see Sec. VII B of Ref. [63]). We simulated lattices of the transversal linear size $L = 64$ and 128 for $L_0 = 16.5$, $L = 128$, and 256 for $L_0 = 32.5$ and $L = 256$ for $L_0 = 64.5$. Given the relatively small correlation length of the film, these transversal extensions should clearly be sufficient to keep finite L effects at a negligible level. This is explicitly verified by the comparison of results obtained for the two different values of L simulated for $L_0 = 16.5$ and 32.5. In the case of $(+,-)$ boundary conditions, the correlation length of the film is monotonically increasing with increasing inverse temperature β. The physical origin of this behavior are fluctuations of the interface between the two phases that arises in the low temperature phase. At the critical point, $\xi_{\rm 2nd,film} \approx 0.212 L_{0,\rm eff}$ [63]. Results for the full range of x that we have studied are given in Fig. 7 of [63]. Here, in order to keep finite L effects negligible, we have chosen $L \gtrapprox 10\xi_{\rm 2nd,film}$. The largest values of L that we simulated are $L = 512$, 1024, and 1024 for $L_0 = 16.5$, 32.5, and 64.5, respectively.

For both $(+,+)$ and $(+,-)$ boundary conditions, we took $i_r = 2$, 4, and 8 for $L_0 = 16.5$, 32.5, and 64.5, respectively. As already mentioned above, we have chosen $n_{\rm exc} = 20$ for all our simulations. As discussed above in Sec. IV B 4, in particular for $L_0 = 64.5$ a larger value of $n_{\rm exc}$ would have been a better choice.

In most of the simulations, we performed 10^5 update cycles. Only for $(+,-)$ for $(L_0, L) = (32.5, 1024)$, $(64.5, 512)$, and $(64.5, 1024)$ we performed less update cycles, where the minimal number was 29 300. In total, we used about 1.5 and 3.5 years of CPU time on a single core of an AMD Opteron 2378 for $(+,+)$ and $(+,-)$ boundary conditions, respectively.

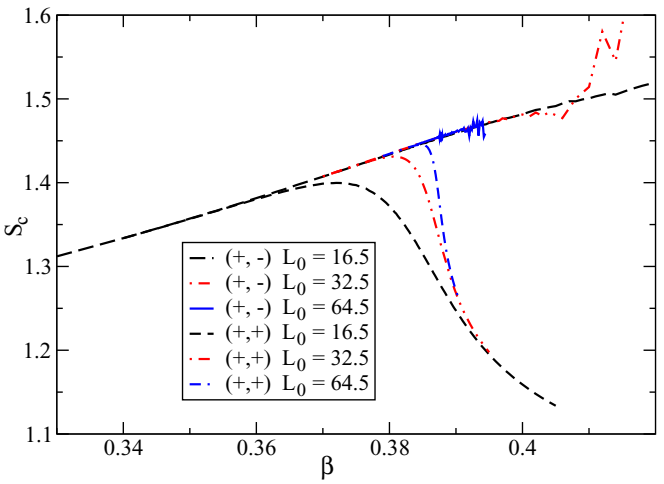

FIG. 2. (Color online) The average size S_c of the frozen exchange clusters per area is plotted as a function of β. We give results for the thicknesses $L_0 = 16.5$, 32.5, and 64.5 for $(+,+)$ and $(+,-)$ boundary conditions.

Before going to the physics results, let us discuss the properties of the exchange cluster algorithm. In Fig. 2, we plot the average size S_c per area of the frozen exchange clusters as a function of β. For small values of β, the curves for both types of boundary conditions as well as all three thicknesses of the film fall on top of each other. For small β, S_c slowly increases with increasing β. In the case of $(+,-)$ boundary conditions S_c increases, up to statistical fluctuations, in the whole range of β that we have studied. In the neighborhood of β_c, no particular change of the behavior can be observed. In Fig. 2, we give no error bars, in order to keep the figure readable. We have convinced ourself that the fluctuations that can be seen for $(+,-)$ boundary conditions for $L_0 = 32.5$ and 64.5 at large values of β can be explained by large statistical errors due to large autocorrelation times. These are likely caused by slow fluctuations of the interface between the phases of opposite magnetization. The analog problem for antiperiodic boundary conditions is discussed in Ref. [86]. Here, we made no attempt to adapt the special cluster algorithm of Ref. [86] to $(+,-)$ boundary conditions.

In the case of $(+,+)$ boundary conditions, starting from a certain value of β that depends on the thickness L_0, S_c departs from the curve for $(+,-)$ boundary conditions. At the resolution of our plot, this happens when the bulk correlation length becomes $\xi \approx L_0/7$. At some $\beta(L_0) < \beta_c$, S_c reaches a maximum. In the low temperature phase, as β increases, again the curves for different L_0 fall on top of each other.

With respect to the performance of the exchange cluster algorithm, it is important to note that in all cases S_c remains small compared with the thickness L_0 in the whole range of β that we have studied.

Next, we discuss how much the statistical error is reduced by employing the improved estimator of the energy difference. Here, we can not use $I_{\rm perf}$ defined in Eq. (34) since we did not perform simulations with $n_{\rm exc} = 0$ for the whole range of β.

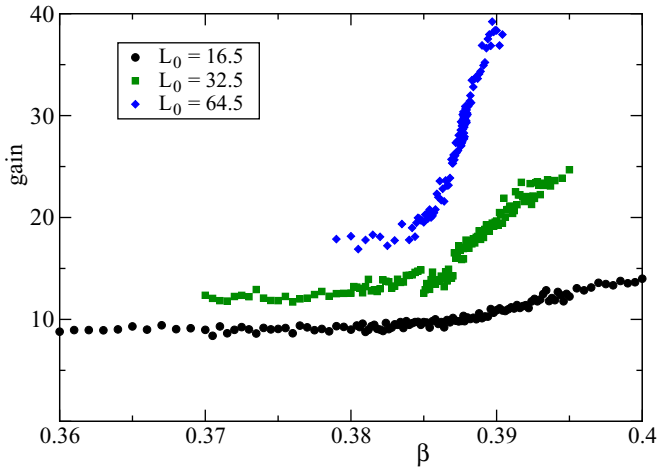

FIG. 3. (Color online) We plot the quantity "gain" defined in Eq. (35) as a function of the inverse temperature β for $(+,+)$ boundary conditions and the thicknesses $L_0 = 16.5$, 32.5, and 64.5.

Hence, we study the ratio

$$\text{gain} = \frac{\epsilon(\Delta E)}{\epsilon(\Delta E_{\text{imp}})}, \tag{35}$$

where $\epsilon(\Delta E)$ and $\epsilon(\Delta E_{\text{imp}})$ are the statistical errors of the energy difference computed in the standard and the improved way, respectively. In the case of the standard estimator we have computed $\epsilon^2[\Delta E(L_0)] = \epsilon^2[E(L_0 + 1/2)] + \epsilon^2[E(L_0 - 1/2)]$ naively, not taking into account the statistical correlation of the two quantities due to the exchange cluster updates. Note that Eq. (35) gives a ratio of statistical errors. Hence, this gain has to be squared to be compared with I_{perf} defined in Eq. (34).

In Fig. 3, this gain is plotted for $(+,+)$ boundary conditions. At small values of β, the gain depends very little on β. At β slightly smaller than β_c the gain starts to increase with β. At larger values of β the gain increases approximately linearly with β. It is interesting to note that the gain increases with increasing thickness of the lattice size. At β_c we get gain $\approx$10.2, 17.3, and 28.5 for $L_0 = 16.5$, 32.5, and 64.5, respectively.

For $(+,-)$ boundary conditions we find that the gain depends only weakly on the inverse temperature β. At β_c we get gain $\approx$8.2, 12.5, and 15.2 for $L_0 = 16.5$, 32.5, and 64.5, respectively. This means that we profit less from the cluster exchange estimator than in the case of $(+,+)$ boundary conditions. The square of gain is quite roughly equal to I_{perf} determined in the section above.

Now, let us turn to the analysis of our numerical results for the thermodynamic Casimir force. Following Refs. [63,68], we chose the starting point β_0 of the integration (13) such that the approximation discussed in Sec. IV A of Ref. [63] is still valid. We get

$$\Delta f_{\text{ex}}(\beta_0) = \pm \frac{C^2(\beta_0)}{\xi^2(\beta_0)} \frac{\exp[-(L_0 + 1 + d/2)/\xi(\beta_0)] - \exp[-(L_0 + 1 - d/2)/\xi(\beta_0)]}{d}, \tag{36}$$

where we have $+$ for $(+,+)$ boundary conditions and $-$ for $(+,-)$ boundary conditions. The numerical values of $C^2(\beta_0)$ and $\xi(\beta_0)$ are taken from Ref. [68]. By comparing results obtained with different choices of β_0 we found that the approximation (36) is accurate at the level of our statistical error for $L_0/\xi(\beta_0) \gtrapprox 8$. To be on the safe side, we used $L_0/\xi(\beta_0) > 10$ in the following.

Let us discuss the results obtained for the scaling function $\theta(x) \simeq -L_{0,\text{eff}}^3 \Delta f_{\text{ex}}$, where $x = t[L_{0,\text{eff}}/\xi_0]^{1/\nu}$. In Fig. 4, we give our results for $(+,-)$ boundary conditions. The data for $L_0 = 64.5$ are attached as Supplemental Material [87]. For $x \gtrapprox -15$, the curves for the three different thicknesses fall nicely on top of each other. For $x \lessapprox -15$, we see a small deviation of the result for $L_0 = 16.5$ from the other two thicknesses. The difference between $L_0 = 32.5$ and 64.5 can hardly be resolved. Hence, we are confident that corrections to scaling are well under control and the numerically important contributions are well described by the effective thickness $L_{0,\text{eff}} = L_0 + L_s$ with $L_s = 1.91(5)$. Finally, let us discuss the maximum of $\theta_{(+,-)}$. Via the zero of ΔE_{ex} we find $\beta_{\text{max}} = 0.392\,560(10)$, $0.389\,512(5)$, and $0.388\,355(3)$ for $L_0 = 16.5$, 32.5, and 64.5, respectively. This corresponds to $x_{\text{max}} = t_{\text{max}}[(L_0 + L_s)/\xi_0]^{1/\nu} = -5.139(11)$[22], $-5.131(14)$[12], and $-5.154(24)$[6], where the number in square brackets gives the error due to the uncertainty of L_s. Note that the dependence on ν essentially cancels when taking into account the dependence of the estimate of ξ_0 on ν [Eq. (5)]. The maximal value of $-L_{0,\text{eff}}^3 \Delta f_{\text{ex}}$ is 6.558(3)[54], 6.561(3)[29], and 6.556(7)[15], where again the number in square brackets gives the error due to the uncertainty of L_s. The results obtained for the different thicknesses nicely agree. We conclude

$$x_{\text{max}} = -5.14(4), \quad \theta_{(+,-)}(x_{\text{max}}) = 6.56(3). \tag{37}$$

These estimates are fully consistent with those of our previous work [68]. Note that the error bars of the final estimates are not reduced compared with [68]. This is mainly due to the fact that the same estimate of L_s is used and that the uncertainty of L_s is a major source of the error.

For a comparison of the result for $\theta_{(+,-)}(x)$ given in Ref. [68], which is fully consistent with the present result, with the results of Monte Carlo simulations of the Ising model [59], experiments on a binary liquid mixture [15], and the extended de Gennes–Fisher local-functional method, see Fig. 1 of Ref. [55].

In Fig. 5, we give our numerical results for $\theta_{(+,+)}(x)$. The data for $L_0 = 64.5$ are attached as Supplemental Material [87]. In the neighborhood of the minimum of $-L_{0,\text{eff}}^3 \Delta f_{\text{ex}}$, the curves for the three different thicknesses fall nicely on top of each other. But, also for small and large values of the scaling variable x, the differences remain small. In particular, the curves for $L_0 = 32.5$ and 64.5 can hardly be discriminated.

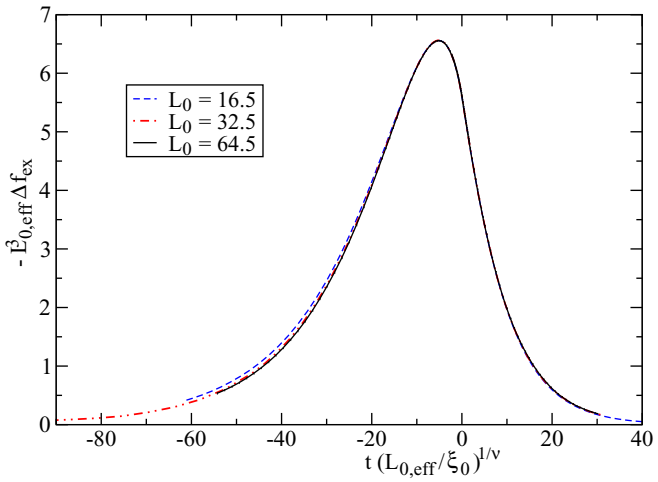

FIG. 4. (Color online) Numerical results for the scaling function $\theta(x)$ for $(+,-)$ boundary conditions. We plot $-L^3_{0,\mathrm{eff}}\Delta f_{\mathrm{ex}}$ as a function of $t(L_{0,\mathrm{eff}}/\xi_0)^{1/\nu}$, where $L_{0,\mathrm{eff}} = L_0 + L_s$ with $L_s = 1.91$, $\xi_0 = 0.2283$, and $\nu = 0.630\,02$. The thicknesses of the film are $L_0 = 16.5$, 32.5, and 64.5. The error bars are typically smaller than the thickness of the lines.

We conclude that similar to the case of $(+,-)$ boundary conditions, corrections to scaling are well under control. Let us look at the minimum of $\theta_{(+,+)}$ in more detail. We find $\beta_{\mathrm{min}} = 0.382\,213(22)$, $0.385\,670(10)$, and $0.387\,001(7)$ for $L_0 = 16.5$, for $L_0 = 16.5$, 32.5, and 64.5, respectively. This corresponds to $x_{\mathrm{min}} = t_{\mathrm{min}}[(L_0 + L_s)/\xi_0]^{1/\nu} = 5.851(23)[25]$, 5.881(29)[14], and 5.866(57)[7], where the number in square brackets gives the error due to the uncertainty of L_s. The minimal value of $-L^3_{0,\mathrm{eff}}\Delta f_{\mathrm{ex}}$ is $-1.755(3)[14]$, $-1.747(4)[8]$, and $-1.750(7)[4]$, where again the number in square brackets gives the error due to the uncertainty of L_s. We conclude

$$x_{\mathrm{min}} = 5.87(7), \quad \theta_{(+,+)}(x_{\mathrm{min}}) = -1.75(1). \tag{38}$$

Also, these estimates are fully consistent with those of our previous work [68].

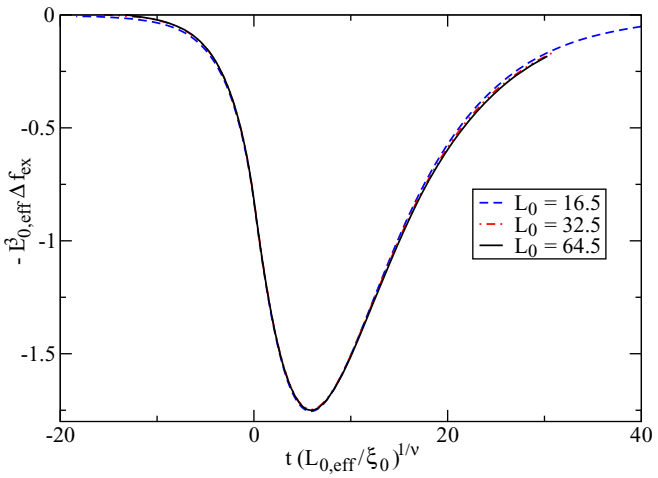

FIG. 5. (Color online) Same as previous figure, but for $(+,+)$ instead of $(+,-)$ boundary conditions.

VI. THERMODYNAMIC CASIMIR FORCE FOR $(O,+)$ BOUNDARY CONDITIONS

The three-dimensional Ising model and the improved Blume-Capel model with $(O,+)$ boundary conditions have been simulated in Refs. [59] and [26,65], respectively. In Ref. [65], we simulated films with $(O,+)$ boundary conditions for the thicknesses $L_0 = 8.5$, 12.5, and 16.5 by using a combination of heat-bath and cluster updates. As transversal extension we took $L = 32$, 48, and 64, respectively. Note that the correlation length of the film is $\xi_{\mathrm{2nd,film}} \approx 0.224(L_0 + L_s)$ at the critical point [65]. Therefore, we expect that finite L effects are small for the values that we had chosen. We performed 10^8, 10^8, and 2×10^8 update cycles for $L_0 = 8.5$, 12.5, and 16.5, respectively. In total, 10 years of CPU time on a single core of an AMD Opteron 2378 were used.

Here, we complement these simulations and study the thicknesses $L_0 = 16.5$ and 24.5 using $L = 64$ and 96, respectively. We used the same type of update cycle as above for $(+,+)$ and $(+,-)$ boundary conditions. In particular, we used $i_r = 2$ and $n_{\mathrm{exc}} = 20$ for $L_0 = 16.5$ and $i_r = 3$ and $n_{\mathrm{exc}} = 20$ for $L_0 = 24.5$. For each value of β we simulated at, 10^7 update cycles were performed. This large number of updates, compared with the study of $(+,-)$ and $(+,+)$ boundary conditions discussed above, is needed to get accurate results for the first and second derivatives of the thermodynamic Casimir force with respect to the surface field h_1. Also, these simulations took about 10 years of CPU time on a single core of an AMD Opteron 2378.

In the case of $(O,+)$ boundary conditions we have the choice, whether we perform the exchange cluster update at the $+$ or the O boundary. Taking the conventions of Secs. II A and IV, this means that we either fix $s_{x,1} = s_{x,2} = 0$ for $x_0 = 0$, $s_{x,1} = 1$ for $x_0 = L_0 + 3/2$, and $s_{x,2} = 1$ for $x_0 = L_0 + 1/2$ or $s_{x,1} = s_{x,2} = 1$ for $x_0 = 0$, $s_{x,1} = 0$ for $x_0 = L_0 + 3/2$, and $s_{x,2} = 0$ for $x_0 = L_0 + 1/2$. In both cases, the frozen clusters have their origin at $x_0 = L_0 + 1/2$. Preliminary tests show that it is preferential to perform the exchange cluster algorithm at the $+$ boundary. In Fig. 6, we give the average size S_c per area of the frozen exchange clusters for $(O,+)$ boundary conditions, where the exchange cluster update is performed at the $+$ boundary. For comparison, we give the analogous result for $(+,+)$ boundary conditions and $L_0 = 16.5$. At high and low values of β, S_c does not depend on the thickness of the film. Furthermore, it coincides with S_c for $(+,+)$ boundary conditions. In the neighborhood of β_c, the behavior of S_c depends on L_0 and furthermore for $L_0 = 16.5$, the behavior for $(+,+)$ and $(O,+)$ boundary conditions is different. We notice that also for $(O,+)$ boundary conditions, S_c remains small compared with the thickness L_0 of the film in the whole range of β that we have simulated.

For comparison, we simulated for $L_0 = 16.5$ with the exchange cluster update performed at the O boundary at 41 values of β, and 4×10^5 update cycles only. In Fig. 13, we plot the resulting S_c. We see that S_c assumes a maximum ≈ 2.12 at $\beta \approx \beta_c$, which is considerably larger than the maximum ≈ 1.42 for the other choice, reached at $\beta \approx 0.38$. At $\beta = 0.34$, which is the smallest inverse temperature that we simulated, S_c is almost equal for the two choices. On the other hand,

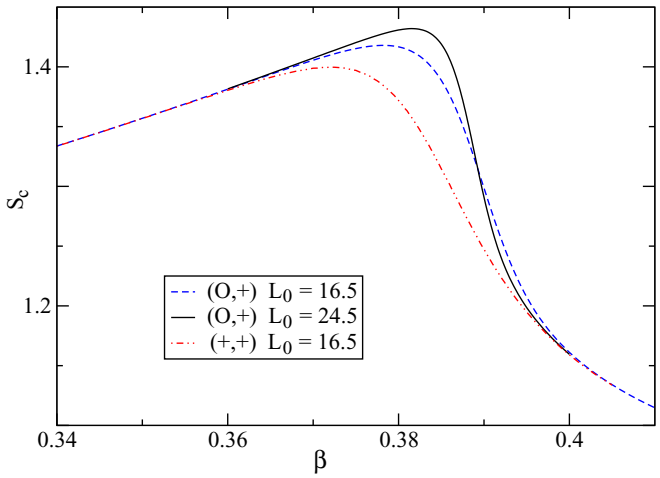

FIG. 6. (Color online) We plot the average size S_c per area of the frozen exchange clusters as a function of β for $(O,+)$ boundary conditions and the thicknesses $L_0 = 16.5$ and 24.5 of the film. For comparison, we give S_c for $(+,+)$ boundary conditions and $L_0 = 16.5$.

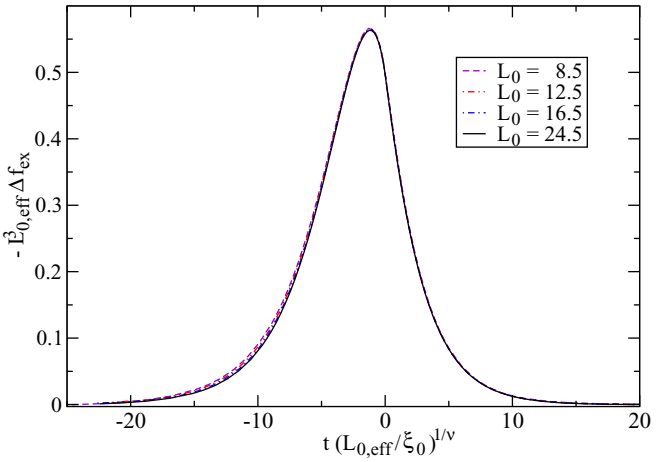

FIG. 8. (Color online) Numerical results for the scaling function $\theta_{(O,+)}(x)$. We plot $-L^3_{0,\mathrm{eff}}\Delta f_{\mathrm{ex}}$ as a function of $t[L_{0,\mathrm{eff}}/\xi_0]^{1/\nu}$, where $L_{0,\mathrm{eff}} = L_0 + L_s$ with $L_s = 1.43$, $\xi_0 = 0.2283$, and $\nu = 0.630\,02$. The thicknesses of the films are $L_0 = 8.5$, 12.5, 16.5, and 24.5. The error bars are typically smaller than the thickness of the lines.

for $\beta = 0.41$, $S_c \approx 1.51$ for the exchange cluster performed at the O boundary, while $S_c \approx 1.11$ for the exchange cluster performed at the $+$ boundary.

In Fig. 7, we plot gain (35) as a function of β. For $L_0 = 16.5$, we give results for both performing the exchange cluster update at the O as well as the $+$ boundary. For $L_0 = 24.5$, only results for performing the exchange cluster update at the $+$ boundary are available. The behavior of gain for the exchange cluster updates at the $+$ boundary is qualitatively very similar to what we have seen above for $(+,+)$ boundary conditions. For $\beta \lessapprox \beta_c$, it depends little on β, while for larger values of β we see a rapid increase of the gain with increasing β. The behavior for the exchange cluster updates at the O boundary is complementary. For $\beta \gtrapprox \beta_c$, the gain increases with decreasing β, while for larger values of β we see only a small increase with increasing β. The intersection between

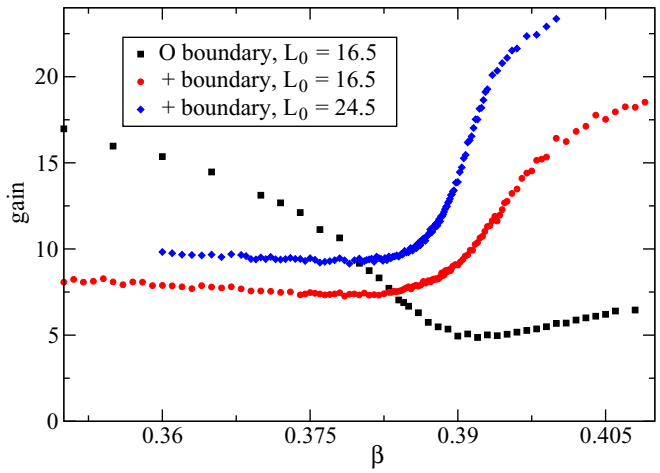

FIG. 7. (Color online) We plot the gain for films with $(O,+)$ boundary conditions. For $L_0 = 16.5$, we performed the exchange cluster update at the O as well as the $+$ boundary. For $L_0 = 24.5$, only exchange cluster updates at the $+$ boundary were performed.

the two gain curves for $L_0 = 16.5$ is located at $\beta \approx 0.383$, where $\xi = 6.643(1)$ [88]. Overall, also taking into account the behavior of S_c, performing the cluster exchange algorithm at the $+$ boundary is the better choice. Both versions of the cluster update clearly reduce the variance of ΔE.

Let us discuss the results for the scaling function of the thermodynamic Casimir force. In Fig. 8, we plot our numerical results for $\theta_{(O,+)}(x)$. The data for $L_0 = 8.5$ and 12.5 are taken from Ref. [65], while those for $L_0 = 16.5$ and 24.5 are computed by using the exchange cluster algorithm. The data for $L_0 = 24.5$ are attached as Supplemental Material [87]. For $x \gtrapprox -5$, the curves fall perfectly on top of each other. For smaller values of x, small differences between the results for different thicknesses can be observed. The scaling function $\theta_{(O,+)}(x)$ shows a maximum in the low temperature phase, very close to the critical point. In order to locate the maximum, we determine the zero of ΔE_{ex}. We find β_{max}=0.390 713(6), 0.389 446(6), 0.388 874 7(15), and 0.388 362 6(10) for $L_0 = 8.5$, 12.5, 16.5, and 24.5, respectively. This corresponds to $x_{\mathrm{max}} = t_{\mathrm{max}}[(L_0 + L_s)/\xi_0]^{1/\nu} = -1.1925(24)[38]$, $-1.1764(41)[27]$, $-1.1743(15)[21]$, and $-1.1723(18)[14]$. For $\theta_{(O,+)}(x_{\mathrm{max}})$, we get the estimates $-\Delta f_{\mathrm{ex}}(\beta_{\mathrm{max}})[L_0 + L_s]^3 = 0.5664(7)[34]$, 0.5657(5)[24], 0.5647(4)[19], and 0.5635(4)[13], where we used $L_s = 1.43(2)$ as input. The number in square brackets gives the error due to the uncertainty of L_s. We see that $-\Delta f_{\mathrm{ex}}(\beta_{\mathrm{max}})[L_0 + L_s]^3$ is monotonically decreasing with L_0 and the error due to the uncertainty of L_s is larger than the statistical one. Therefore, we performed a fit, leaving L_s as free parameter. We get, taking all four thicknesses into account, $\theta_{(O,+)}(x_{\mathrm{max}}) = 0.5636(23)$ and $L_s = 1.41(2)$, which is consistent with our previous estimate of L_s. As our final estimate, we quote

$$x_{\mathrm{max}} = -1.168(5), \quad \theta_{(O,+)}(x_{\mathrm{max}}) = 0.5635(20), \tag{39}$$

where we extrapolated x_{max} linearly in L_0^{-2} to $L_0 \to \infty$. The error bar of x_{max} is chosen such that the estimate

obtained for $L_0 = 24.5$ is included. In the case of $\theta_{(O,+),\max}$, the estimate obtained for $L_0 = 24.5$ and our fit essentially coincide, which leads to our final estimate. Our present estimates are compatible with $x_{\max} = -1.174(10)$ and $\theta_{(O,+),\max} = 0.564(3)$ [65], and the error bars are slightly reduced. For a summary of previous results, we refer the reader to Sec. VI C of Ref. [65]. At the critical point, we get $-\Delta f_{\rm ex}(\beta_{\max})[L_0 + L_s]^3 = 0.4978(7)$[30], 0.4982(6)[21], 0.4976(4)[17], and 0.4964(3)[11] for $L_0 = 8.5$, 12.5, 16.5, and 24.5, respectively, where again we used $L_s = 1.43(2)$ as input. The value for $L_0 = 24.5$ is slightly smaller than that for $L_0 = 8.5$, 12.5, and 16.5. Mainly based on the result for $L_0 = 24.5$, we quote

$$\theta_{(O,+)}(0) = 0.496(2) \tag{40}$$

as our final result, which is fully consistent with $\theta_{(O,+)}(0) = 0.497(3)$ obtained in Ref. [65] and with $\theta_{(O,+)}(0) = 0.492(5)$ given in Eq. (34) of Ref. [26].

Next, let us turn to the derivatives of the thermodynamic Casimir force per area with respect to the surface field h_1. The thermodynamic Casimir force per area as a function of the inverse temperature β and the surface field h_1 follows the scaling law

$$F_{\rm Casimir}(\beta,h_1) = k_B T L_0^{-d} \Theta_{(O,+)}\big(x, x_{h_1}\big), \tag{41}$$

where

$$x_{h_1} = h_1 [L_0/l_{\rm ex,nor,0}]^{y_{h_1}}, \tag{42}$$

where for our model $l_{\rm ex,nor,0} = 0.213(3)$ [Eq. (73) of [65]], and the surface critical RG-exponent $y_{h_1} = 0.7249(6)$ [Eq. (52) of [65]]. In particular, for a vanishing surface field we get the scaling function

$$\theta_{(O,+)}(x) = \Theta_{(O,+)}(x,0) \tag{43}$$

discussed above.

Following Ref. [65], we compute the Taylor expansion of the thermodynamic Casimir force with respect to the boundary field h_1 around $h_1 = 0$ up to the second order. To this end, we compute the first and second derivatives of $\Delta f_{\rm ex}$ with respect to h_1. The nth derivatives can be written as

$$\frac{\partial^n \Delta f_{\rm ex}(L_0,\beta,h_1)}{\partial h_1^n} = -\int_{\beta_0}^{\beta} d\tilde\beta \frac{\partial^n \Delta E_{\rm ex}(L_0,\tilde\beta,h_1)}{\partial h_1^n}, \tag{44}$$

where

$$\frac{\partial^n \Delta E_{\rm ex}(L_0,\beta,h_1)}{\partial h_1^n} = \frac{\partial^n \langle E\rangle_{(L_0+1/2,\beta,h_1)}}{\partial h_1^n} - \frac{\partial^n \langle E\rangle_{(L_0-1/2,\beta,h_1)}}{\partial h_1^n}. \tag{45}$$

Note that there is no bulk contribution since the internal energy of the bulk does not depend on h_1. In the Monte Carlo simulation, the first derivative can be computed as

$$\frac{\partial \langle E\rangle_{(L_0,\beta,h_1)}}{\partial h_1} = \langle E M_1\rangle - \langle E\rangle\langle M_1\rangle, \tag{46}$$

where

$$M_1 = \sum_{x_1,x_2} s_{(1,x_1,x_2)}. \tag{47}$$

The second derivative is given by

$$\frac{\partial^2 \langle E\rangle_{(L_0,\beta,h_1)}}{\partial h_1^2} = \big\langle E M_1^2\big\rangle - 2\langle E M_1\rangle\langle M_1\rangle - \langle E\rangle\big\langle M_1^2\big\rangle + 2\langle E\rangle\langle M_1\rangle^2. \tag{48}$$

Higher derivatives could be computed in a similar way. However, it turns out that the relative statistical error of the second derivative is much larger than that of the first one. Therefore, we abstain from implementing higher derivatives.

We computed the quantities (46) and (48) with reduced variance by using the exchange cluster update. Here, we did not work out an explicit expression as Eq. (31) for ΔE. Instead, we implemented Eq. (30) directly for the observables that enter Eqs. (46) and (48). In order to avoid a numerical effort that is proportional to the volume of the film, we kept track of the values of E of the two films, while exchange cluster updating and performing the Todo-Suwa updates of the i_r layers.

In the case of $L_0 = 16.5$, we can compare with our results obtained in Ref. [65], where we performed 20 times more measurements. Using the cluster exchange update, we have reduced the statistical error of $\frac{\partial \Delta E_{\rm ex}(L_0,\tilde\beta,h_1)}{\partial h_1}$ by a factor slightly larger than 2 for $\beta \lessapprox \beta_c$ compared with the result of Ref. [65]. In the low temperature phase, this factor increases up to ≈ 6 at $\beta = 0.405$. For the second derivative with respect to h_1 a similar reduction of the statistical error can be observed.

In Fig. 9, we plot our results for $\theta'_{(O,+)}(x) \equiv \frac{\partial \Theta_{(O,+)}(x,x_{h_1})}{\partial h_1}|_{h_1=0}$. The curves for different thicknesses fall nicely on top of each other. One observes that in contrast to $\theta(x)$, $\theta'(x)$ has a large amplitude also for $x \geqslant 0$. In particular, the minimum is located close to the critical point, in the high temperature phase. The analysis of the data gives $\beta_{\min} = 0.384\,04(5)$, $0.385\,75(3)$, $0.386\,44(2)$, and $0.387\,020(10)$ for $L_0 = 8.5$, 12.5, 16.5, and 24.5, respectively. This corresponds to $x_{\min} = 1.468(20)$[5], 1.345(20)[3], 1.305(20)[2], and 1.284(18)[2], where again the number in

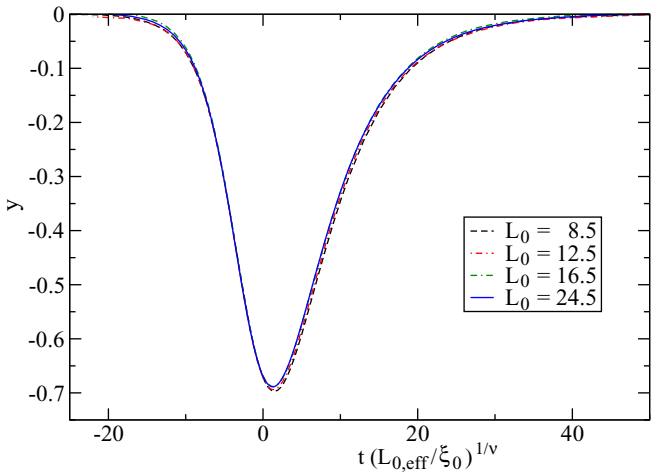

FIG. 9. (Color online) We plot $y = -L_{0,\rm eff}^3 (L_{0,\rm eff}/l_{\rm ex,nor,0})^{-y_{h_1}} \frac{\partial \Delta f_{\rm ex}}{\partial h_1}$ as a function of $t(L_{0,\rm eff}/\xi_0)^{1/\nu}$ for $(O,+)$ boundary conditions for the thicknesses $L_0 = 8.5$, 12.5, 16.5, and 24.5. To this end, we have used $L_{0,\rm eff} = L_0 + L_s$ with $L_s = 1.43$, $\xi_0 = 0.2283$, $\nu = 0.63002$, $l_{\rm ex,nor,0} = 0.213$, and $y_{h_1} = 0.7249$.

square brackets gives the error due to the uncertainty of L_s. Still, we see a small trend in the numbers. Therefore, we extrapolated linearly in $1/L_0^2$, arriving at $x_{\min} = 1.253(16)$. For $-L_{0,\mathrm{eff}}^3 (L_{0,\mathrm{eff}}/l_{\mathrm{ex,nor},0})^{-y_{h_1}} \frac{\partial \Delta f_{\mathrm{ex}}}{\partial h_1}$, with $L_{0,\mathrm{eff}} = L_0 + L_s$ we get at the minimum the values $-0.697(1)[3]\{7\}$, $-0.694(2)[2]\{7\}$, $-0.691(1)[2]\{7\}$, and $-0.689(1)[1]\{7\}$ for $L_0 = 8.5$, 12.5, 16.5, and 24.5, respectively. Here the number in square brackets gives again the error due to the uncertainty of L_s, while the number in curly brackets gives the error induced by the uncertainty of $l_{\mathrm{ex,nor},0}$. It turns out that the latter is dominating. As our final result, we quote

$$x_{\min} = 1.25(4), \quad \theta'_{(O,+)}(x_{\min}) = -0.689(3)\{7\}. \tag{49}$$

As final estimate of $x_{\min}$, we took our extrapolation and the error bar is chosen such that the result for $L_0 = 24.5$ is still included. As final estimate of $\theta'_{(O,+),\min}$, we simply took the result obtained for $L_0 = 24.5$. The error bar given in parentheses is mainly motivated by the comparison with the result for $L_0 = 16.5$. The dominant error given in curly brackets is due to the uncertainty of $l_{\mathrm{ex,nor},0}$. Our present estimates are consistent with and slightly more accurate than those given in Ref. [65].

In Fig. 10, we plot our results for $\theta''_{(O,+)}(x) \equiv \frac{\partial^2 \Theta_{(O,+)}(x,x_{h_1})}{\partial h_1^2}|_{h_1=0}$. Here, the error bars are, despite the variance reduction, larger than the thickness of the lines. For $L_0 = 12.5$, taken from Ref. [65], and $L_0 = 24.5$ we give the error bars. For $L_0 = 8.5$ and 16.5 we omit them to keep the figure readable. The curves for different thicknesses fall reasonably well on top of each other. The discrepancies might be attributed to the statistical error. The function displays a single maximum. Analyzing the data, we arrive at the final result

$$x_{\max} = -2.0(1), \quad \theta''_{(O,+)}(x_{\max}) = 0.41(1)\{1\}. \tag{50}$$

The number given in curly brackets gives the error due to the uncertainty of $l_{\mathrm{ex,nor},0}$. Again, our result is consistent with Ref. [65].

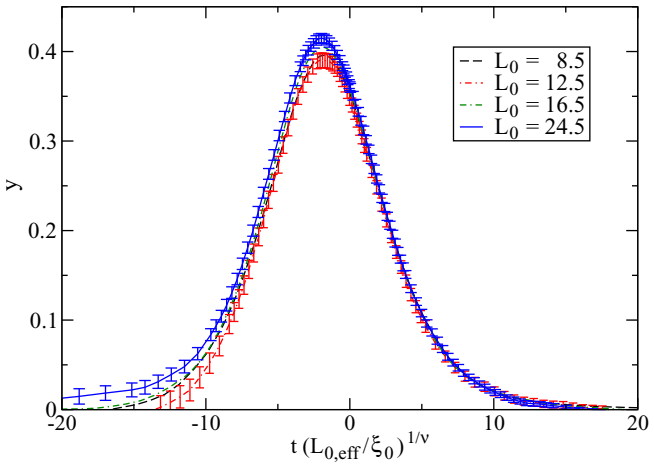

FIG. 10. (Color online) We plot $y = -L_{0,\mathrm{eff}}^3 (L_{0,\mathrm{eff}}/l_{\mathrm{ex,nor},0})^{-2y_{h_1}} \frac{\partial^2 \Delta f_{\mathrm{ex}}}{\partial h_1^2}$ as a function of $t(L_{0,\mathrm{eff}}/\xi_0)^{1/\nu}$ for $(O,+)$ boundary conditions for the thicknesses $L_0 = 8.5$, 12.5, 16.5, and 24.5. To this end, we have used $L_{0,\mathrm{eff}} = L_0 + L_s$ with $L_s = 1.43$, $\xi_0 = 0.2283$, $\nu = 0.63002$, $l_{\mathrm{ex,nor},0} = 0.213$, and $y_{h_1} = 0.7249$.

We have demonstrated that also the statistical error of the derivatives of $\langle \Delta E \rangle$ with respect to the boundary field h_1 can be reduced by using the exchange cluster update. As a result, we reduced the errors of the scaling function $\theta_{(O,+)}(x)$, $\theta'_{(O,+)}(x)$, and $\theta''_{(O,+)}(x)$ with respect to Ref. [65]. This, however, leaves the conclusions of Ref. [65] unchanged. Therefore, we refer the reader to Ref. [65] for a detailed discussion. A particularly interesting observation is that for a finite boundary field h_1, the thermodynamic Casimir force might change sign as a function of the thickness L_0.

VII. FILMS WITH (O,O) BOUNDARY CONDITIONS

In contrast to the cases studied above, (O,O) boundary conditions do not break the global $\mathbb{Z}_2$ symmetry of the system. Therefore, films with (O,O) boundary conditions are expected to undergo a second order phase transition that belongs to the universality class of the two-dimensional Ising model. At this transition, the correlation length of the film diverges and we therefore expect large finite size effects, where the finiteness in the transversal directions is meant. This should also affect the thermodynamic Casimir force. This problem has been discussed in Ref. [59] and for the case of films with periodic boundary conditions in Ref. [67]. Here, we put this discussion on a quantitative level. Since the transition belongs to the two-dimensional Ising universality class, we can make use of the universal finite size scaling function of the free energy density that we compute in Sec. VII A by using the exact solution of the two-dimensional Ising model [89]. In Sec. VII B, in order to make use of this universal function, we accurately determine the transition temperature and match the scaling variable for a large range of thicknesses of the film. Finally, in Sec. VII C we compute the thermodynamic Casimir force for $L_0 = 8.5$, 12.5, 16.5, and 24.5 by using the exchange cluster algorithm. The algorithm seems to fail in reducing the variance in the low temperature phase of the films. We suggest to remediate this problem by breaking by hand the $\mathbb{Z}_2$ symmetry in the low temperature phase. Still, in the neighborhood of the transition of the film, we benefit only little from the exchange cluster update.

A. Finite size effects in the neighborhood of the 2D transition

The reduced Hamiltonian of the Ising model on the square lattice in the absence of an external field is given by

$$H = -\beta \sum_{\langle xy \rangle} s_x s_y, \tag{51}$$

where $s_x \in \{-1,1\}$ and $\langle xy \rangle$ is a pair of nearest neighbor sites. For the discussion of the critical behavior of the Ising model on the square lattice, it is convenient to introduce

$$\tau = \frac{1}{2}\left(\frac{1}{\sinh 2\beta} - \sinh 2\beta\right) \tag{52}$$

as reduced temperature. The exponential correlation length in the thermodynamic limit behaves as

$$\xi \simeq \xi_{0,\pm} |\tau|^{-\nu}, \tag{53}$$

where $\nu = 1, \xi_{0,+} = 1/\sqrt{2}$, and $\xi_{0,-} = \xi_{0,+}/2$, where $\xi_{0,+}$ and $\xi_{0,-}$ are the amplitudes of the exponential correlation length in the high and the low temperature phases, respectively.

The reduced free energy density in the thermodynamic limit is given by [90]

$$f(\tau) = -\tfrac{1}{2}\ln(2\cosh^2 2\beta) + f_{\rm sing}(\tau), \tag{54}$$

where

$$f_{\rm sing}(\tau) = -\int_0^\pi \frac{d\theta}{2\pi}\ \ln\left[1 + \left(1 - \frac{\cos^2\theta}{1+\tau^2}\right)^{1/2}\right]. \tag{55}$$

In the neighborhood of the critical point, the reduced free energy density behaves as

$$f(\tau) \simeq \frac{1}{2\pi}\tau^2 \ln|\tau| + A(\tau), \tag{56}$$

where $A(\tau)$ is an analytic function.

Here, we are interested in the finite size scaling behavior of the reduced free energy density

$$f(\beta, L) = -\frac{1}{L^2}\ln Z(\beta, L), \tag{57}$$

where $L = L_1 = L_2$ is the linear extension of the lattice and periodic boundary conditions are assumed. To this end, we have numerically evaluated Eq. (39) of Ref. [89]. The differences

$$\Delta f_2(\beta, L) = f(\beta, 2L) - f(\beta, L) \tag{58}$$

and

$$\Delta f_\infty(\beta, L) = f(\beta, \infty) - f(\beta, L) \tag{59}$$

are governed by finite size scaling functions

$$g_n(\tau L) \simeq \Delta f_n(\beta, L) L^2. \tag{60}$$

We have constructed the function g_2 numerically by evaluating Eq. (39) of Ref. [89]. In order to get g_∞, Eq. (54) is used in addition. Our results obtained for $L = 1024$ are given in Fig. 11. Comparing with results for smaller L, we conclude that the deviation of our result for $L = 1024$ from the asymptotic limit is less than 10^{-6}.

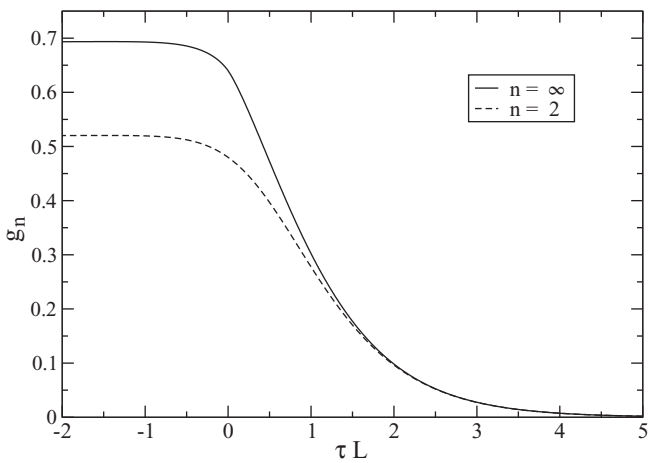

FIG. 11. Finite size scaling function $g_n(\tau L)$ obtained by evaluating the free energy density of the Ising model on the square lattice with periodic boundary conditions for $L = 1024$.

B. Phase transition of films with (O, O) boundary conditions

The transition is expected to be of second order and to share the universality class of the two-dimensional Ising model. This allows us to take advantage of exact results obtained for the two-dimensional Ising model and conformal field theory. In our numerical study, we shall follow the approach of Ref. [75], where films of the Ising model with periodic boundary conditions were studied.

We determine the inverse transition temperature $\beta_{c,2D}(L_0)$ by finite size scaling. For simplicity, we consider lattices with $L_1 = L_2 = L$. An estimate $\bar\beta_{c,2D}(L_0, L)$ of $\beta_{c,2D}(L_0)$ is given by the solution of

$$R(\beta, L_0, L) = R^*, \tag{61}$$

where $R(\beta, L_0, L)$ is a renormalization group invariant quantity like the Binder cumulant U_4, the second moment correlation length over the lattice size ξ_{2nd}/L, or the ratio of partition functions $R_Z = Z_a/Z_p$, where Z_a is the partition function of a system with periodic boundary conditions in 1-direction and antiperiodic boundary conditions in 2-direction, while Z_p is the partition function of a system with periodic boundary in both 1- and 2-directions. The fixed point value R^* is defined by

$$R^* := \lim_{L\to\infty} R(\beta_{c,2D}, L_0, L). \tag{62}$$

It can be obtained, e.g., from the study of the two-dimensional Ising model. It is known to high numerical precision for ξ_{2nd}/L and U_4 [91]. The fixed point value of R_Z is exactly known for arbitrary ratios L_1/L_2. It can be derived both from the exact solution of the two-dimensional Ising model [89] as well as from conformal field theory. For $L_1 = L_2$ one gets

$$R_Z^* = 0.372\,884\,880\,824\,589\ldots. \tag{63}$$

The estimate of the inverse critical temperature converges as

$$\bar\beta_{c,2D}(L_0, L) - \beta_{c,2D}(L_0) = c(L_0) L^{-1/\nu_{2D}-\omega} + \cdots, \tag{64}$$

where $\nu_{2D} = 1$ is the critical exponent of the correlation length of the two-dimensional Ising universality class. In the case of ξ_{2nd}/L and U_4 we have effectively $\omega = 1.75$ due to the analytic background of the magnetic susceptibility. For R_Z, the leading correction is caused by the breaking of the rotational symmetry by the lattice, resulting in $\omega = 2$. For a detailed discussion of corrections to scaling in two-dimensional Ising models, see e.g. Ref. [92]. Therefore, following Ref. [75], we determine $\bar\beta_{c,2D}(L_0, L)$ by using the ratio R_Z of partition functions.

We determined the coefficients of the Taylor expansion of the quantities we were interested in up to the third order around the inverse temperature β_s, where we simulated at. We have chosen β_s as good approximation of $\bar\beta_{c,2D}(L_0, L)$. This estimate is obtained by preliminary simulations, or from results for smaller lattice sizes that we had simulated already. We solved Eq. (61) by replacing $R(\beta, L_0, L)$ on the left side of the equation by its third order Taylor expansion around β_s.

We simulated films of a thickness up to $L_0 = 64$ and a transversal lattice size up to $L = 1024$. In most cases, we performed 10^6 update cycles. One cycle consists of one

TABLE II. Numerical results for $\bar{\beta}_{c,2D}(L_0,L)$ [Eq. (61)] and the slope over the linear lattice size $\bar{S}/L$ [Eq. (66)] for the thicknesses $L_0 = 4$ and 8 for a large range of transversal lattice sizes L.

L_0	L	$\bar{\beta}_{c,2D}$	$-\frac{1}{L}\frac{\partial R_Z}{\partial \beta}\vert_{R_Z=R_Z^*}$
4	8	0.4395281(25)	2.45398(26)
4	12	0.4396433(18)	2.49361(30)
4	16	0.4396701(14)	2.50712(33)
4	24	0.4396820(10)	2.51720(38)
4	32	0.43968400(72)	2.51981(41)
4	48	0.43968644(50)	2.52385(45)
4	64	0.43968672(40)	2.52391(48)
4	128	0.43968708(20)	2.52453(54)
4	256	0.43968704(18)	2.5259(11)
8	16	0.4072021(10)	3.7970(5)
8	24	0.40723203(69)	3.8380(6)
8	32	0.40723991(53)	3.8520(6)
8	48	0.40724338(37)	3.8621(7)
8	64	0.40724454(27)	3.8664(8)
8	128	0.40724568(20)	3.8710(12)
8	512	0.40724571(12)	3.8750(38)

heat-bath sweep, one Todo-Suwa [84] sweep, a Swendsen-Wang [83] cluster update, and a wall-cluster [93] update plus a measurement of Z_a/Z_p for each of the two directions. In total, these simulations took about 2 years of CPU time on a single core of a Quad-Core AMD Opteron(tm) 2378 CPU.

In Table II, we give the results obtained for $L_0 = 4$ and 8 for a large range of L. Here we performed 10^8 update cycles, except for $L_0 = 4$, $L = 256$ where we performed 3.3×10^7 update cycles, and $L_0 = 8$, 128, and 512 where we performed 5.5×10^7 and 9.6×10^6 update cycles, respectively. Fitting the data with the ansatz

$$\bar{\beta}_{c,2D}(L_0,L) = \beta_{c,2D}(L_0) + cL^{-3} \tag{65}$$

we get, taking all data into account, $\beta_{c,2D}(4) = 0.439\,687\,10(12)$, $c = -0.080(1)$, and $\chi^2/\text{d.o.f.} = 1.16$, and $\beta_{c,2D}(8) = 0.407\,245\,61(9)$, $c = -0.181(4)$, and $\chi^2/\text{d.o.f.} = 1.39$ for $L_0 = 4$ and 8, respectively. Note that for $L_0 = 4$ and 8 for $L \geqslant 16L_0$, the estimate of $\bar{\beta}_{c,2D}(L_0,L)$ is consistent with $\beta_{c,2D}(L_0)$ within the statistical error. Therefore, in the following, for other thicknesses L_0 we took $\bar{\beta}_{c,2D}(L_0,L)$ with $L \gtrapprox 16L_0$ as our final estimate of $\beta_{c,2D}(L_0)$.

In order to match the reduced temperature of the two-dimensional Ising model and the reduced temperature of the film, the derivative of R_Z with respect to the reduced temperature t at R_Z^* is a useful quantity. Taking $\partial R_Z/\partial t = -\partial R_Z/\partial\beta$ at R_Z^* means that the derivative is taken at $\bar{\beta}$, which is the solution of Eq. (61). It behaves as

$$\bar{S} := -\left.\frac{\partial R_Z}{\partial \beta}\right|_{R_Z=R_Z^*} = aL^{1/\nu_{2D}}\ (1 + cL^{-\omega} + \cdots). \tag{66}$$

In the fourth column of Table II we give $\bar{S}/L$ for $L_0 = 4$ and 8 for all L we have simulated. We fitted these data with the ansatz

$$\bar{S}/L = a + bL^{-2}. \tag{67}$$

TABLE III. Numerical results for the phase transition of films with (O,O) boundary conditions. The thickness of the film is given by L_0 and L is the linear extension in the two transversal directions. In the third column, we give our estimate of the inverse of the transition temperature $\beta_{c,2D}(L_0)$ as defined by Eq. (61). In the fourth column, we give $\bar{S}/L$ as defined by Eq. (66).

L_0	L	$\beta_{c,2D}$	$-\frac{1}{L}\frac{\partial R_Z}{\partial \beta}\vert_{R_Z=R_Z^*}$
4	256	0.43968704(18)	2.5259(11)
5	160	0.4258884(15)	2.903(7)
6	384	0.41724094(59)	3.256(9)
7	112	0.4114039(17)	3.579(8)
8	512	0.40724571(12)	3.875(4)
9	300	0.40416349(61)	4.157(11)
10	256	0.40180434(69)	4.430(12)
11	256	0.39995347(66)	4.669(13)
12	192	0.39846789(82)	4.918(13)
13	192	0.39725856(81)	5.147(14)
14	256	0.39625624(59)	5.391(15)
15	256	0.39541461(57)	5.568(16)
16	256	0.39470035(55)	5.789(16)
17	256	0.39408852(54)	6.048(17)
24	384	0.39148514(31)	7.350(23)
25	384	0.39125639(31)	7.524(24)
32	512	0.39013763(21)	8.661(29)
48	768	0.38900912(12)	10.988(46)
64	1024	0.38854284(8)	12.973(52)

Taking all data for $L_0 = 4$ into account, we get $a = 2.525\,02(18)$, $b = 4.546(22)$, and $\chi^2/\text{d.o.f.} = 1.17$, while fitting all data for $L_0 = 8$ we get $a = 3.8708(4)$, $b = 18.91(19)$, and $\chi^2/\text{d.o.f.} = 0.68$. In the case of $L_0 = 8$, we find that $\bar{S}/L$ for $L = 128$ and 512 is consistent with the asymptotic result obtained from the fit. For $L_0 = 4$, this is the case only for $L = 128$ and 256. For $L = 64$, we see a deviation of about two standard deviations. In Table III, we give our final estimates of $\beta_{c,2D}$ and the slope $\bar{S}/L$ for all thicknesses L_0 that we have simulated. We took results obtained for $L \gtrapprox 16L_0$ as our final estimate. Note that for other values of L_0, the statistics is considerably smaller and therefore the statistical errors larger than for $L_0 = 4$ and 8.

The transition temperature of the film approaches the transition temperature of the three-dimensional bulk system as the thickness L_0 of the film increases. Based on standard RG arguments, one expects [79,94]

$$\beta_{2D,c}(L_0) - \beta_{3D,c} \simeq aL_0^{-1/\nu}. \tag{68}$$

It turns out that corrections to scaling have to be included to fit our data. First, we allowed for an effective thickness of the film

$$\beta_{c,2D}(L_0) - \beta_{c,3D} = a[L_0 + L_s]^{-1/\nu}, \tag{69}$$

where we fixed $\beta_{c,3D} = 0.387\,721\,735$ and $\nu = 0.630\,02$. The parameters of the fit are a and L_s. Taking into account only thicknesses $L_0 \geqslant 24$ we still get $\chi^2/\text{d.o.f.} = 2.91$. Therefore, we added a term that takes into account the leading analytic

TABLE IV. Fitting the data of Table III with the ansatz (70), where $\beta_{c,\mathrm{bulk}} = 0.387\,721\,735$ and $\nu = 0.630\,02$ are fixed, while a, b, and L_s are the parameters of the fit. Data for thicknesses $L_0 \geqslant L_{0,\mathrm{min}}$ are taken into account.

$L_{0,\mathrm{min}}$	a	b	L_s	χ^2/d.o.f.
6	0.61841(5)	0.546(5)	0.9665(18)	3.41
7	0.61815(7)	0.505(9)	0.9570(29)	1.23
8	0.61813(7)	0.502(9)	0.9560(29)	1.12
9	0.61806(7)	0.485(12)	0.9513(37)	0.97
10	0.61799(8)	0.467(17)	0.9467(46)	0.85
11	0.61797(10)	0.462(22)	0.9453(61)	0.93
12	0.61791(11)	0.440(30)	0.9401(77)	0.91

correction

$$\beta_{c,2\mathrm{D}}(L_0) - \beta_{c,3\mathrm{D}} = a[L_0 + L_s]^{-1/\nu} + b[L_0 + L_s]^{-2/\nu}, \tag{70}$$

where now b is an additional parameter of the fit. We find that already for $L_{0,\mathrm{min}} = 8$, where all data for $L_0 \geqslant L_{0,\mathrm{min}}$ are taken into account, χ^2/d.o.f. ≈ 1. Hence, the ansatz (70) along with the numerical values of the parameters given in Table IV can be used to obtain estimates of $\beta_{c,2\mathrm{D}}(L_0)$ for thicknesses $8 \leqslant L_0 \leqslant 64$, where we have not simulated at. One should note that the parameters have a clear dependence on the value of ν that is used. For example, fixing $\nu = 0.629\,92$ we get for $L_{0,\mathrm{min}} = 10$ the results $a = 0.618\,75(8)$, $L_s = 0.9569(48)$, 0.4931(17), and χ^2/d.o.f. $= 0.83$. An important observation is that the results obtained for L_s are fully consistent with $L_s = 0.96(2)$ obtained in Ref. [65] by studying the magnetization profile of films with $(O,+)$ boundary conditions at the critical point. In terms of the scaling variable, we get

$$x_c = -a\xi_0^{-1/\nu} = -6.444(10), \tag{71}$$

where we have taken into account the uncertainties of ν and β_c.

In Ref. [95], the authors computed $\beta_{c,2\mathrm{D}}$ for the Ising model on the simple cubic lattice, using the crossing of the Binder cumulant. They obtain $\beta_{c,2\mathrm{D}} = 0.258\,44(4)$, $0.242\,89(3)$, $0.235\,87(2)$, $0.232\,09(3)$, $0.229\,65(3)$, and $0.228\,04(3)$ for the thicknesses $L_0 = 4$, 6, 8, 10, 12, and 14, respectively. In the case of the Ising model, we expect that corrections proportional to $L_0^{-\omega}$ with $\omega = 0.832(6)$ contribute significantly, making the extrapolation to $L_0 \to \infty$ more difficult than in the case of the improved Blume-Capel model. Despite this fact, to get at least a rough answer, we fitted the Ising data with the ansatz (69), using $\beta_{c,3\mathrm{D}} = 0.221\,654\,62(2)$ [see Eq. (A2) of [68]]. We find $a = 0.480(4)$, $L_s = 1.18(5)$, and χ^2/d.o.f. $= 0.95$ taking into account all data for $L_0 \geqslant 8$. Using the estimate of ξ_0 given in Eq. (A10) of [68] we get $x_c = -6.37(5)$, which is close with our estimate obtained for the improved Blume-Capel model. Equation (12) of Ref. [38] gives $x_c \approx -6.5$ for the Ising universality class, which is in excellent agreement with our result.

Finally, we studied the behavior of $\bar{S}/L$ at the critical point as a function of the thickness L_0 of the film. It behaves as

$$\bar{S}/L \simeq a\,[L_0 + L_s]^{1/\nu - 1}. \tag{72}$$

Performing various fits, using $L_s = 0.96(2)$ and $\nu = 0.630\,02(10)$ as input, we arrive at $a = 1.12(1)$. In terms of the scaling variable $x = t[(L_0 + L_s)/\xi_0]^{1/\nu}$, this means

$$\bar{S}_x := \frac{\partial R_Z}{\partial x} = \bar{S}[(L_0 + L_s)/\xi_0]^{-1/\nu} L \simeq a\xi_0^{1/\nu} \frac{L}{L_0 + L_s} = 0.1074(10) \frac{L}{L_0 + L_s}. \tag{73}$$

For the transversal correlation length of the film in the high temperature phase, Eq. (53) translates to

$$\xi_{\mathrm{film}} \simeq 1.99(2)[L_0 + L_s](x - x_c)^{-1} \tag{74}$$

using

$$\lim_{L\to\infty} [\bar{S}/L]_{2\mathrm{D\ Ising}} = \lim_{L\to\infty} \frac{1}{L} \left.\frac{\partial Z_a/Z_p}{\partial \tau}\right|_{\tau=0} = 0.302\,124\,710\,040\,7\ldots \tag{75}$$

for the two-dimensional Ising model.

In Fig. 12, we plot $\bar{U}_4$ as a function of $L/(L_0 + L_s)$, where $\bar{U}_4$ is the Binder cumulant $U_4 = \frac{\langle m^4\rangle}{\langle m^2\rangle^2}$ at $R_Z = R_Z^*$, where $m = \sum_x s_x$ is the magnetization. Following Ref. [91], $U_4^* = 1.167\,922\,9 \pm 0.000\,004\,7$. It is interesting to see that already starting from $L_0 = 4$, finite L effects nicely scale with the effective thickness $L_0 + L_s$. We have checked that the decay of corrections with increasing L is consistent with $\bar{U}_4 - U_4^* \propto L^{-7/4}$, as theoretically expected. Finally, we convinced ourself that $\bar{\xi}_{2\mathrm{nd}}/L$ converges to $(\xi_{2\mathrm{nd}}/L) = 0.905\,048\,829\,2 \pm 0.000\,000\,000\,4$ [91] as $L/(L_0 + L_s) \to \infty$. These observations strongly support the hypothesis that the transition of the film, for any thickness L_0, belongs to the two-dimensional Ising universality class.

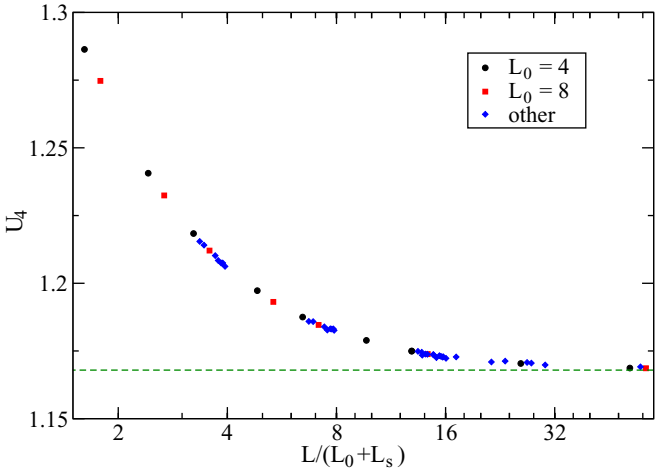

FIG. 12. (Color online) We plot $\bar{U}_4$ as a function of $L/(L_0 + L_s)$ with $L_s = 0.96$. For comparison, we give $U_4^* = 1.167\,922\,9$ as green dashed line. The data points for $L_0 = 4$ and 8 are given as black circles and red squares, respectively. For all other thicknesses, the data points are shown as blue diamonds. The error bars are smaller than the size of the symbols. For the definition of the quantities and a discussion, see the text.

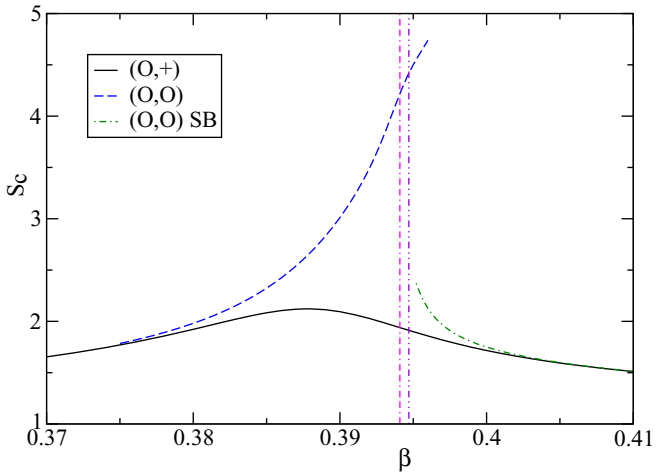

FIG. 13. (Color online) We plot the size of the frozen exchange clusters S_c for the thickness $L_0 = 16.5$. We compare $(O,+)$ and (O,O) boundary conditions. In case of (O,O), we give results for the simulation with and without breaking of the $\mathbb{Z}_2$ symmetry. The vertical lines give the inverse transition temperature of films of the thickness $L_0 = 16$ and 17.

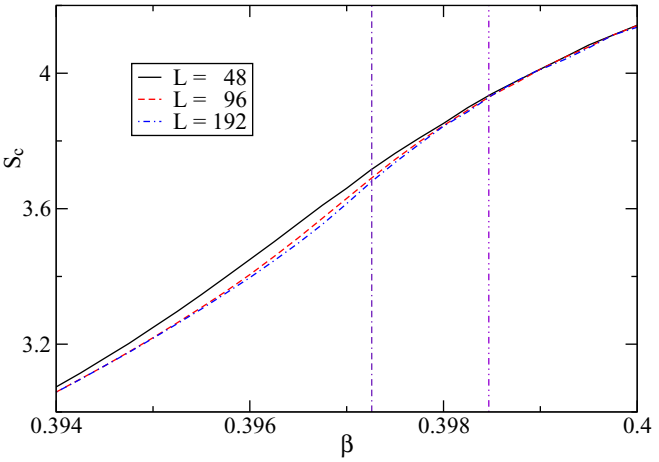

FIG. 14. (Color online) We plot the size of the frozen exchange clusters S_c for the thickness $L_0 = 12.5$ for the three transversal extensions $L = 48$, 96, and 192.

C. Thermodynamic Casimir force for (O,O) boundary conditions

The thermodynamic Casimir force for (O,O) boundary conditions has been studied for the Ising model [59] and the improved Blume-Capel model [26]. We have simulated films of the thicknesses $L_0 = 8.5$, 12.5, 16.5, and 24.5. For the parameters of the update, we took $n_{\rm exc} = 20$ throughout and $i_r = 1$, 2, 2, and 3 for $L_0 = 8.5$, 12.5, 16.5, and 24.5, respectively. We simulated the transversal lattices sizes $L =$ 32, 64, 128, and 256 for $L_0 = 8.5$, $L = 48$, 96, and 192 for $L_0 = 12.5$, $L = 64$ for $L_0 = 16.5$, and $L = 96$ and 192 for $L_0 = 24.5$. For all thicknesses, we simulated at slightly more than hundred values of β in the neighborhood of the bulk critical point. The larger transversal lattice sizes were simulated at less values of β than the smaller ones, focusing at the neighborhood of the transition of the film. We performed 10^6 update cycles for each value of β and most lattice sizes. Exceptions are $(L_0,L) = (8.5,256)$ and $(12.5,192)$ were we performed only 2×10^5 update cycles. In total, we used about 5 years of CPU time on a single core of an AMD Opteron 2378 running at 2.4 GHz.

Let us first discuss the performance of the exchange cluster algorithm. In Fig. 13, we plot the average size per area of the frozen exchange clusters S_c for $L_0 = 16.5$ and $L = 64$. For comparison, we give our result for $(O,+)$ boundary conditions, where the exchange cluster update is performed at the O boundary. For small β, the curves for $(O,+)$ and (O,O) boundary conditions fall on top of each other. While for $(O,+)$ boundary conditions a maximum is reached at $\beta \approx \beta_c$, for (O,O) ones we find that S_c is growing monotonically with increasing β. At the inverse transition temperatures of the two films, S_c is already a significant fraction of the thickness L_0 of the film. We find $S_c \approx 3.25$, 3.82, 4.32, and 5.15 at $\beta = [\beta_{c,2D}(L_0 + 1/2) + \beta_{c,2D}(L_0 - 1/2)]/2$, for $L_0 = 8.5$, 12.5, 16.5, and 24.5, respectively. For those thicknesses, where we have simulated more than one value of L, we find at $\beta_{c,2D}$ and in a certain neighborhood below a small dependence of S_c on L. In Fig. 14, we plot as an example S_c for $L_0 = 12.5$ and $L = 48$, 96, and 192.

Looking at the simulation in the low temperature phase in detail, we find that the large frozen exchange clusters grow, when the magnetization of the two systems have different sign. Physically, one could force the two systems to have the same sign by applying a bulk field h, such that $hL_0L^2m \gg 1$, where m is the magnetization of the film. The larger L, the smaller the amplitude of the bulk field h could be chosen. At the end, one would extrapolate the results obtained to $h = 0$. Here instead, we break the symmetry by hand. After the sweeps with the heat bath and the Todo-Suwa algorithm and the Swendsen-Wang cluster update of the two systems, before starting the $n_{\rm exc}$ exchange cluster updates, we forced the two systems to positive or zero magnetization. To this end, we multiplied all spins of a system with -1, if its magnetization is negative. This is certainly an update of the configuration that does not fulfill balance and hence we introduce a systematic error. However, we expect that this error vanishes in the limit $L \to \infty$ and also decreases as we go deeper into the symmetry broken phase. In Fig. 13, we also give S_c for simulations with this explicit symmetry breaking (SB). We find that indeed S_c is much smaller than for the simulation without SB. Also, in the low temperature phase of the films, S_c is now decreasing with increasing β. For large β, the curve is falling on top of that for $(O,+)$ boundary conditions.

Let us briefly discuss the gain (35) that we do not plot here. Without SB, for all L_0 that we studied, it is almost linearly decreasing with increasing β, until $\beta_{c,2D}(L_0 + 1/2)$ is reached. Starting from this point, it stays roughly constant with a value that is approximately equal to 1.4. For $\beta \approx 0.389$ gain takes about the same value 4 for all thicknesses that we study. Using SB, starting from β above $\beta_{c,2D}(L_0 - 1/2)$, the gain rapidly increases with increasing β. For example, the gain reaches the value 5 at $\beta \approx 0.421$, 0.403, 0.3973, and 0.3925 for $L_0 = 8.5$, 12.5, 16.5, and 24.5, respectively.

For β somewhat larger than $\beta_{c,2D}$, we simulated with SB and without. For example, for $L_0 = 8.5$ we find that the

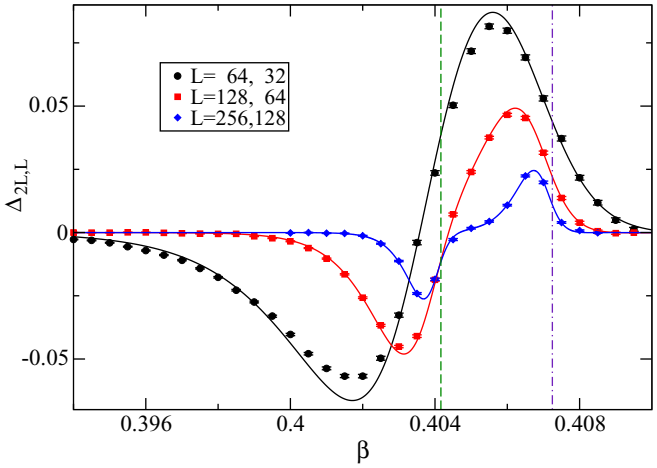

FIG. 15. (Color online) We plot $\Delta_{2L,L} = \Delta E(L_0,2L) - \Delta E(L_0,L)$ for $L_0 = 8.5$. Our numerical data are given by black circles, red squares and blue diamonds for $L = 32$, 64 and 128, respectively. The solid lines give the theoretical prediction, obtained from the universal finite size scaling function of the free energy density of the 2D Ising transition. The vertical dashed green line indicates the phase transition for $L_0 = 9$ and the vertical dashed-dotted violet line the phase transition for $L_0 = 8$.

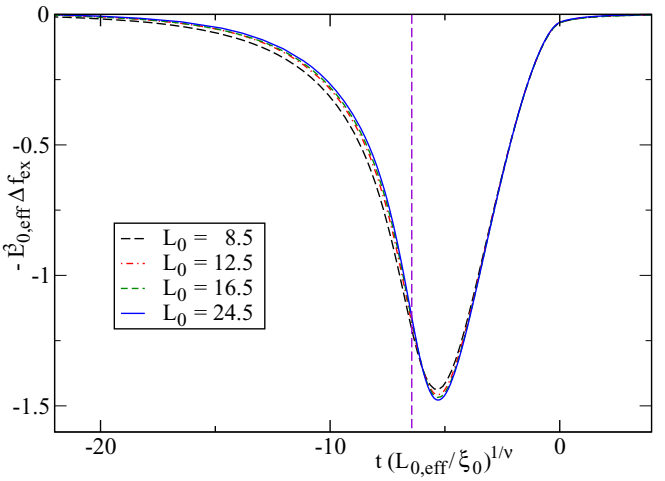

FIG. 16. (Color online) We plot $-L^3_{0,\mathrm{eff}}\Delta f_{\mathrm{ex}}$ as function of $t(L_{0,\mathrm{eff}}/\xi_0)^{1/\nu}$ for $(L_0,L) = (8.5,32)$, $(12.5,48)$, $(16.5,64)$, and $(24.5,96)$, where we used $L_{0,\mathrm{eff}} = L_0 + L_s$ with $L_s = 0.96$, $\xi_0 = 0.2283$, and $\nu = 0.630\,02$. The vertical dashed violet line gives the position of the phase transition of the film.

results for ΔE are consistent at the level of our statistical accuracy starting from $\beta = 0.409$, 0.408, 0.4075, and 0.407 for $L = 32$, 64, 128, and 256, respectively. In our analysis of the thermodynamic Casimir force below, we have used the results obtained with SB starting from slightly larger values of β, to have a safety margin.

In a first step of the analysis we check whether finite L effects in ΔE_{ex} are well described by the universal finite size scaling function g_n [Eq. (60)]. In Fig. 15, we plot $\Delta_{2L,L} = \Delta E(L_0,2L) - \Delta E(L_0,L)$ for $L_0 = 8.5$ and $L = 32$, 64, and 128. Note that $\Delta E(L_0,2L) - \Delta E(L_0,L) = \Delta E_{\mathrm{ex}}(L_0,2L) - \Delta E_{\mathrm{ex}}(L_0,L)$ since the bulk energy density cancels. Our numerical results are compared with the prediction obtained from the universal finite size scaling function g_2. As input, we use the inverse transition temperature $\beta_{c,2\mathrm{D}}$ and the slope of R_Z at R_Z^* given in Table III, and Eq. (75):

$$[E(L_0,2L) - E(L_0,L)]_{\mathrm{predict}} = -\frac{d}{d\beta} g_2\{c\,[\beta_{c,2\mathrm{D}}(L_0) - \beta]\,L\}L^{-2}, \qquad (76)$$

where

$$c = \frac{[\bar{S}/L]_{\mathrm{film},L_0}}{[\bar{S}/L]_{2\mathrm{D\ Ising}}}. \qquad (77)$$

We find that for $L = 32$ the data are quite close to the prediction obtained from the universal finite size scaling function g_2. Note that for $(L_0,L) = (12.5,48)$ and $(24.5,96)$ similar observations can be made. Going to $L = 64$ the matching between the data points and the predicted behavior becomes better. Only at the minimum and the maximum of the curve a small mismatch can be observed. For $L_0 = 12.5$ and $L = 96$, a similar observation can be made. Finally, for $L = 128$, at the level of our statistical accuracy, the match between the data points and the predicted behavior is perfect.

Next, we checked how the results for the thermodynamic Casimir force are scaling with the thickness L_0 of the film. To this end, we plot in Fig. 16 our numerical results for $-(L_0 + L_s)^3\Delta f_{\mathrm{ex}}$ as function of $t[(L_0 + L_s)/\xi_0]^{1/\nu}$ for $(L_0,L) = (8.5,32)$, $(12.5,48)$, $(16.5,64)$, and $(24.5,96)$. Since $L/[L_0 + L_s]$ is similar for these lattices, we expect that finite $L/[L_0 + L_s]$ corrections to scaling are similar. For $x \gtrapprox -3$, the curves fall almost perfectly on top of each other. In contrast, for smaller values of x, the different curves can be resolved at our level of numerical accuracy. In particular, the one for $L_0 = 8.5$ is clearly different from the others. Since the difference between the results for $L_0 = 16.5$ and 24.5 is rather minute, we expect that for $L_0 = 24.5$ deviations from the scaling limit are of a similar size as our statistical errors for $L_0 = 24.5$. A more quantitative discussion of corrections will be given below, when we analyze the position of the minimum of the scaling function θ.

Finally, in Fig. 17 we plot $-(L_0 + L_s)^3\Delta f_{\mathrm{ex}}$ as function of $t[(L_0 + L_s)/\xi_0]^{1/\nu}$ for $L_0 = 24.5$ for $L = 96$ and 192 and our extrapolation of the $L = 192$ result to $L \to \infty$ obtained by using the universal scaling function g_∞. The extrapolated data are attached as Supplemental Material [87]. We see that the minimum of θ deepens as the lattice size increases and the position of the minimum approaches x_c. The position of the minimum for $L \to \infty$ is close to x_c but definitely different from it. We extrapolated our results obtained for $L_0 = 8.5$, $L = 256$ and $L_0 = 12.5$, $L = 192$ to $L = \infty$. Note that for $L_0 = 16.5$ we have only data for $L = 64$, and therefore a reliable extrapolation is not possible. Analyzing these data, we find that $(x_{\min},\theta_{\min}) = [-5.771(2)[19], -1.6922(4)[108]]$, $[-5.757(5)[14], -1.6924(8)[76]]$, and $[-5.746(7)[7], -1.6925(10)[40]]$ for $L_0 = 8.5$, 12.5, and 24.5, respectively. Again, the number in square brackets gives the error due to the uncertainty of L_s. As our final result for the limit $L_0 \to \infty$, we quote

$$x_{\min} = -5.75(2), \quad \theta_{(O,O)}(x_{\min}) = -1.693(5), \qquad (78)$$

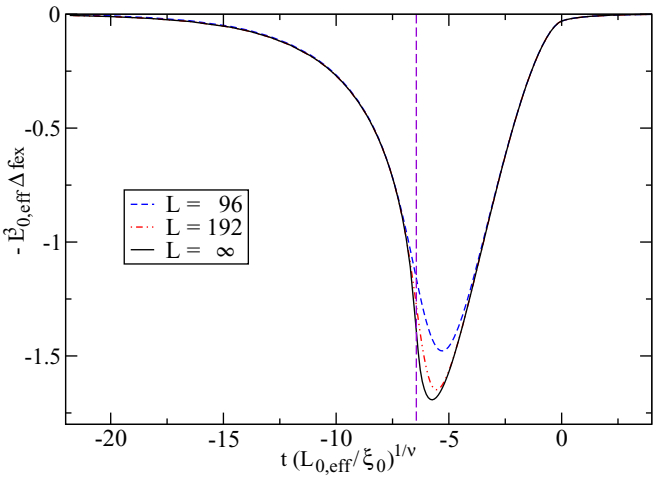

FIG. 17. (Color online) We plot $-L_{0,\mathrm{eff}}^3 \Delta f_{\mathrm{ex}}$ as function of $t(L_{0,\mathrm{eff}}/\xi_0)^{1/\nu}$ for $L_0 = 24.5$ for $L = 96$ and 192 and our extrapolation to $L \to \infty$. We used $L_{0,\mathrm{eff}} = L_0 + L_s$ with $L_s = 0.96$, $\xi_0 = 0.2283$, and $\nu = 0.630\,02$. The vertical dashed violet line indicates x_c.

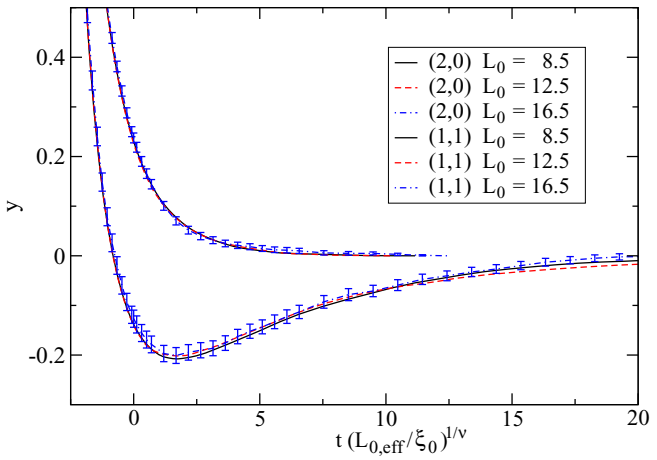

FIG. 18. (Color online) We plot $y^{(2,0)} = -L_{0,\mathrm{eff}}^3 (L_{0,\mathrm{eff}}/l_{\mathrm{ex,nor},0})^{-2y_{h_1}} \frac{\partial^2 \Delta f_{\mathrm{ex}}}{\partial h_1^2}$ and $y^{(1,1)} = -L_{0,\mathrm{eff}}^3 (L_{0,\mathrm{eff}}/l_{\mathrm{ex,nor},0})^{-2y_{h_1}} \frac{\partial^2 \Delta f_{\mathrm{ex}}}{\partial h_1 \partial h_2}$ at $h_1 = h_2 = 0$ as a function of $t(L_{0,\mathrm{eff}}/\xi_0)^{1/\nu}$ for (O,O) boundary conditions for the thicknesses $L_0 = 8.5$, 12.5, and 16.5. To this end, we have used $L_{0,\mathrm{eff}} = L_0 + L_s$ with $L_s = 0.96$, $\xi_0 = 0.2283$, $\nu = 0.630\,02$, $l_{\mathrm{ex,nor},0} = 0.213$, and $y_{h_1} = 0.7249$. To keep the figure readable, error bars are only shown for $L_0 = 16.5$, where they are the largest. We use the same types of lines for $y^{(2,0)}$ and $y^{(1,1)}$. Note that $y^{(1,1)} < y^{(2,0)}$ in the whole range that is plotted.

which is consistent with the results obtained for the three different thicknesses.

Since $x_{\min}$ is definitely larger than $x_c = -6.444(10)$, the correlation length of the film at $x_{\min}$ is finite. Following Eq. (74), $\xi_{\mathrm{Film}}(x_{\min}) \approx 1.99 \times (-5.75 + 6.444)\, L_{0,\mathrm{eff}} \approx 1.4 L_{0,\mathrm{eff}}$. For $L \gtrapprox 10 \xi_{\mathrm{Film}}$, finite L effects should be small. Hence, for $L \gtrapprox 14\, L_0$ the features of the minimum of θ should be essentially independent of L. This is consistent with the observations of Ref. [26] (see in particular their Fig. 16). Obviously, in an experiment no periodic boundary conditions can be applied. Still, $\xi_{\mathrm{Film}}(x_{\min})$ indicates how large the transversal linear size of the system should be to avoid finite size effects.

Our result can be compared with Ref. [59] who simulated the Ising model on the simple cubic lattice and the thicknesses $L_0 = 7.5$, 11.5, 15.5, and 19.5. Throughout, they used $\rho = L_0/L = 1/6$. They arrive at $(x_{\min}, \theta_{\min}) = [-5.74(2), -1.629(3)]$ and $[-5.73(4), -1.41(1)]$, depending on whether they use their Eqs. (18), (20), or (21) to extrapolate to $L_0 \to \infty$. Interpolating our data to $\rho = 1/6$ using the universal finite size scaling function of the free energy, we arrive at $x_{\min} \approx -5.46$ and $\theta_{\min} \approx -1.61$. Hence, the apparently good agreement of $x_{\min}$ with our result seems to be a coincidence. The authors of Ref. [26] give no explicit result for $x_{\min}$ and $\theta_{\min}$ in the text. From the inset of their Fig. 16 we read off $x_{\min} \approx -5.5(1)$ and $\theta_{\min} \approx -1.66(5)$. The main reason for the larger error bar of [26] compared with us is that they use $L_s = 0.8(2)$, c' in their notation, instead of our $L_s = 0.96(2)$. Using field theoretic methods, the author of Ref. [38] arrives at $x_{\min} \approx -5.53$ and $\theta_{\min} \approx -1.5$.

Similar to Eq. (41), the thermodynamic Casimir force per area as a function of the inverse temperature β and the surface fields h_1 and h_2 follows the scaling law

$$F_{\mathrm{Casimir}}(\beta, h_1, h_2) = k_B T L_0^{-d} \Theta_{(O,O)}(x, x_{h_1}, x_{h_2}), \qquad (79)$$

where

$$x_{h_1} = h_1 [L_0/l_{\mathrm{ex,nor},0}]^{y_{h_1}}, \quad x_{h_2} = h_2 [L_0/l_{\mathrm{ex,nor},0}]^{y_{h_1}}, \qquad (80)$$

where for our model $l_{\mathrm{ex,nor},0} = 0.213(3)$ [Eq. (73) of [65]] and the surface critical RG exponent $y_{h_1} = 0.7249(6)$ [Eq. (52) of [65]].

The partial derivatives of Δf_{ex} with respect to h_1 and h_2 at $h_1 = h_2 = 0$ are determined in a similar fashion as for $(O,+)$ boundary conditions. In the high temperature phase of the film, due to the $\mathbb{Z}_2$ symmetry of the problem, the first derivatives vanish. In Fig. 18, we plot our results for

$$\theta^{(1,1)}(x) \equiv \left. \frac{\partial^2 \Theta(x, x_{h_1}, x_{h_2})}{\partial x_{h_1} \partial x_{h_2}} \right|_{x_{h_1} = x_{h_2} = 0}$$
$$\simeq -L_{0,\mathrm{eff}}^3 (L_{0,\mathrm{eff}}/l_{\mathrm{ex,nor},0})^{-2y_{h_1}} \frac{\partial^2 \Delta f_{\mathrm{ex}}}{\partial h_1 \partial h_2} \qquad (81)$$

and

$$\theta^{(2,0)}(x) \equiv \left. \frac{\partial^2 \Theta(x, x_{h_1}, x_{h_2})}{\partial x_{h_1}^2} \right|_{x_{h_1} = x_{h_2} = 0}$$
$$\simeq -L_{0,\mathrm{eff}}^3 (L_{0,\mathrm{eff}}/l_{\mathrm{ex,nor},0})^{-2y_{h_1}} \frac{\partial^2 \Delta f_{\mathrm{ex}}}{\partial h_1^2}. \qquad (82)$$

Despite variance reduction, the statistical error increases rapidly with increasing thickness. Our data for $L_0 = 24.5$ already have a quite large statistical error and we therefore did not plot them in Fig. 18. In the high temperature phase of the bulk system, only $\theta^{(1,1)}$ has a significant amplitude and it is negative. Going to lower temperatures, towards the transition temperature of the film, both $\theta^{(1,1)}$ and $\theta^{(2,0)} = \theta^{(0,2)}$ rapidly increase. Also, $\theta^{(1,1)}$ and $\theta^{(2,0)} = \theta^{(0,2)}$ approach each other in this range. As a result, in this range, the thermodynamic

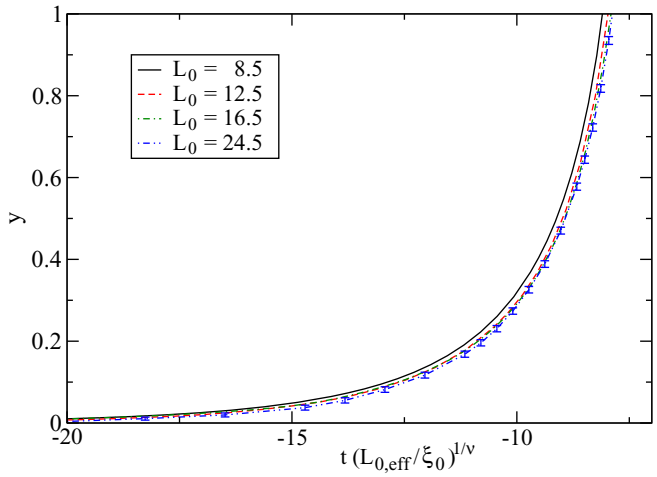

FIG. 19. (Color online) We plot $y = -L_{0,\mathrm{eff}}^3 (L_{0,\mathrm{eff}}/l_{\mathrm{ex,nor},0})^{-y_{h_1}} \frac{\partial \Delta f_{\mathrm{ex}}}{\partial h_1}$ as a function of $t(L_{0,\mathrm{eff}}/\xi_0)^{1/\nu}$ for (O,O) boundary conditions for the thicknesses $L_0 = 8.5$, 12.5, 16.5, and 24.5 for the low temperature phase of the film. To this end, we have used $L_{0,\mathrm{eff}} = L_0 + L_s$ with $L_s = 0.96$, $\xi_0 = 0.2283$, $\nu = 0.630\,02$, $l_{\mathrm{ex,nor},0} = 0.213$, and $y_{h_1} = 0.7249$.

Casimir force varies much less with h_1 for $h_1 = -h_2$ than, for example, for $h_1 = h_2$.

At the minimum of $\theta_{(O,O)}$ we have $\theta^{(2,0)} \approx \theta^{(1,1)} \approx 500$. This means that, for example, for $h_1 = h_2$, already for $x_{h_1} \gtrapprox 0.03$ the characteristics of the thermodynamic Casimir force for (O,O) boundary conditions are completely wiped out.

For completeness, we also give our results for temperatures below the transition temperature of the film. Here, we rely on our simulations with SB. Since the $\mathbb{Z}_2$ symmetry is broken, the first derivative with respect to x_{h_1} does not vanish. The numerical integration is started at large values of β. Our

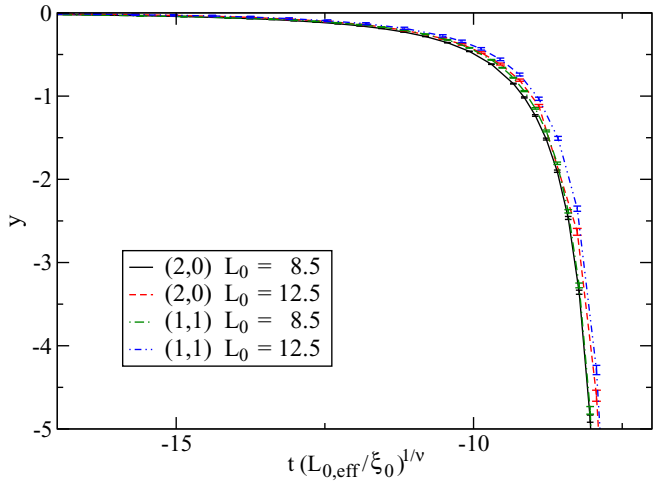

FIG. 20. (Color online) We plot $y^{(2,0)} = -L_{0,\mathrm{eff}}^3 (L_{0,\mathrm{eff}}/l_{\mathrm{ex,nor},0})^{-2y_{h_1}} \frac{\partial^2 \Delta f_{\mathrm{ex}}}{\partial h_1^2}$ and $y^{(1,1)} = -L_{0,\mathrm{eff}}^3 (L_{0,\mathrm{eff}}/l_{\mathrm{ex,nor},0})^{-2y_{h_1}} \frac{\partial^2 \Delta f_{\mathrm{ex}}}{\partial h_1 \partial h_2}$ as a function of $t(L_{0,\mathrm{eff}}/\xi_0)^{1/\nu}$ for (O,O) boundary conditions for the thicknesses $L_0 = 8.5$ and 12.5 in the low temperature phase of the film. To this end, we have used $L_{0,\mathrm{eff}} = L_0 + L_s$ with $L_s = 0.96$, $\xi_0 = 0.2283$, $\nu = 0.630\,02$, $l_{\mathrm{ex,nor},0} = 0.213$, and $y_{h_1} = 0.7249$.

numerical data are plotted in Fig. 19. For $L_0 = 12.5$, 16.5, and 24.5, we find a quite good collapse of the data on a single scaling curve. The function θ' is positive in the whole range $x < x_c$. It rapidly increases as x_c is approached.

Finally, in Fig. 20 we plot our results for the second derivatives of the scaling function with respect to the scaling variables. Here, the statistical errors are quite large and grow rapidly with the thickness of the film. Therefore, we give only results for $L_0 = 8.5$ and 12.5. In the whole range $x < x_c$, we find that $\theta^{(1,1)} \approx \theta^{(2,0)}$. The functions are negative and the amplitude increases rapidly as x_c is approached.

Our results can be compared with those of [66], who studied films with finite values of h_1 and h_2. In particular, in their Figs. 7 and 8 they give results for $h_1 = |h_2|$ and $h_2 = 0$, respectively. Their results for small $\tilde{h}_1$ are essentially consistent with ours. Matching their data with ours, we get $\tilde{h}_1 \approx 0.9 x_{h_1}$ for the relation between the scaling variables that are used.

VIII. CONCLUSIONS AND OUTLOOK

We study the thermodynamic Casimir force by using Monte Carlo simulations of lattice models. In particular, we are concerned with the bulk universality class of the three-dimensional Ising model, which for example characterizes a continuous demixing transition of fluid binary mixtures. In Ref. [73], we used the exchange cluster algorithm, or geometric cluster algorithm [74], to study the thermodynamic Casimir force between a spherical object and a plane substrate. The main point of the exchange cluster algorithm applied to this problem is that it allows us to define a variance reduced estimator for the difference of the internal energy of two systems that are characterized by slightly different distances between the spherical object and the substrate. In the case of the sphere-plate geometry, it turned out to be mandatory to use this variance reduced estimator to get a meaningful result for the thermodynamic Casimir force by using the approach discussed by Hucht [57].

Here, we go one step back and apply the exchange cluster algorithm to the film or plate-plate geometry. For this geometry, quite satisfactory numerical results were obtained already. A long list of references is given in the Introduction. We simulate the improved Blume-Capel model on the simple cubic lattice with $(+,+)$, $(+,-)$, $(O,+)$, and (O,O) boundary conditions, where $+$ and $-$ are strongly symmetry breaking boundary conditions and O stands for the ordinary surface universality class. For a discussion of these boundary conditions, see the Introduction and Sec. II. We demonstrate that also for the film geometry, the exchange cluster algorithm allows for a considerable reduction of the variance. The only exception are films with (O,O) boundary conditions in the direct neighborhood of the transition of the film. This allowed us to simulate films with a larger thickness than before, allowing us to consolidate previous results. Our final estimates for the thermodynamic Casimir force only moderately improve on previous estimates. This is due to the fact that the remaining errors mainly stem from quantities such as L_s (see Sec. II) and $l_{\mathrm{ex,nor},0}$ [see Eq. (42)] that were used as input. These quantities were taken from previous work and are computed by analyzing

physical quantities different from the thermodynamic Casimir force.

In Sec. IV, we discuss that the exchange cluster algorithm can be applied to a larger class of boundary conditions than simulated here. In particular, enhanced surface couplings or finite surface fields could be studied. Quite recently, the authors of [69,70] computed the thermodynamic Casimir force in the presence of an external bulk field. To this end, one can compute the difference in the excess free energy per area by integrating the difference in the excess magnetization per area over the external field [70], where the difference is taken for films of thickness $L_0 + 1/2$ and $L_0 - 1/2$. The integration is started at a strong external field, where the difference in the excess free energy vanishes. Alternatively, one might start at a vanishing external field, where the difference in the excess free energy per area is known from previous simulations. It seems likely that the exchange cluster algorithm allows us to reduce the variance of the difference in the excess magnetization in such studies. Furthermore, one could think of applications different from the thermodynamic Casimir force. For example, one could compute the free energy of defects. It would be interesting to check whether the simulation of spin glass models could be speeded up by exchanging spins between replica.

The emphasis of our physics analysis is on (O, O) boundary conditions. Films with such boundary conditions are expected to undergo a second order phase transition in the universality class of the two-dimensional Ising model. This transition has been studied for the Ising model on the simple cubic lattice for thicknesses up to $L_0 = 14$ in Ref. [95]. Here, we obtain accurate results for thicknesses up to $L_0 = 64$ using the finite size scaling approach discussed in Ref. [75]. Our numerical results nicely confirm the expectation that the transition belongs to the universality class of the two-dimensional Ising model. We compute the finite size scaling function g_n [Eq. (60)] that governs the finite size scaling behavior of the free energy density in the universality class of the two-dimensional Ising model for $n = 2$ and ∞. We show that finite L effects in the thermodynamic Casimir force, where L is the extension of the film in the transversal directions, are described by g_n. In particular, using g_∞, our knowledge of the inverse transition temperature of the film and the numerical matching of the scaling variable, we extrapolate our results for the thermodynamic Casimir force to $L \to \infty$. For details, see Sec. VII C. This approach could also be applied to other types of boundary conditions that do not break the $\mathbb{Z}_2$ symmetry of the problem, in particular, to periodic boundary conditions or enhanced surface couplings that allow us to study the special surface universality class.

ACKNOWLEDGMENT

This work was supported by the Deutsche Forschungsgemeinschaft (DFG) under the Grant No. HA 3150/3-1.

[1] M. E. Fisher and P.-G. de Gennes, C. R. Seances Acad. Sci., Ser. B **287**, 207 (1978).
[2] H. B. G. Casimir, Proc. K. Ned. Akad. Wet., Ser. B: Phys. Sci. **51**, 793 (1948).
[3] K. G. Wilson and J. Kogut, Phys. Rep. C **12**, 75 (1974).
[4] M. E. Fisher, Rev. Mod. Phys. **46**, 597 (1974).
[5] M. E. Fisher, Rev. Mod. Phys. **70**, 653 (1998).
[6] A. Pelissetto and E. Vicari, Phys. Rep. **368**, 549 (2002).
[7] M. Krech, *The Casimir Effect in Critical Systems* (World Scientific, Singapore, 1994).
[8] K. Binder, in *Phase Transitions and Critical Phenomena*, edited by C. Domb and J. L. Lebowitz (Academic, London, 1983), Vol. 8.
[9] H. W. Diehl, in *Phase Transitions and Critical Phenomena*, edited by C. Domb and J. L. Lebowitz (Academic, London, 1986), Vol. 10, p. 76.
[10] H. W. Diehl, Int. J. Mod. Phys. B **11**, 3503 (1997).
[11] R. Garcia and M. H. W. Chan, Phys. Rev. Lett. **83**, 1187 (1999).
[12] R. Garcia and M. H. W. Chan, Phys. Rev. Lett. **88**, 086101 (2002).
[13] T. Ueno, S. Balibar, T. Mizusaki, F. Caupin, and E. Rolley, Phys. Rev. Lett. **90**, 116102 (2003).
[14] A. Ganshin, S. Scheidemantel, R. Garcia, and M. H. W. Chan, Phys. Rev. Lett. **97**, 075301 (2006).
[15] M. Fukuto, Y. F. Yano, and P. S. Pershan, Phys. Rev. Lett. **94**, 135702 (2005).
[16] S. Rafaï, D. Bonn, and J. Meunier, Phys. A (Amsterdam) **386**, 31 (2007).
[17] C. Hertlein, L. Helden, A. Gambassi, S. Dietrich, and C. Bechinger, Nature (London) **451**, 172 (2008).
[18] F. Soyka, O. Zvyagolskaya, Ch. Hertlein, L. Helden, and C. Bechinger, Phys. Rev. Lett. **101**, 208301 (2008).
[19] A. Gambassi, A. Maciołek, C. Hertlein, U. Nellen, L. Helden, C. Bechinger, and S. Dietrich, Phys. Rev. E **80**, 061143 (2009).
[20] U. Nellen, L. Helden, and C. Bechinger, Europhys. Lett. **88**, 26001 (2009).
[21] M. Tröndle, O. Zvyagolskaya, A. Gambassi, D. Vogt, L. Harnau, C. Bechinger, and S. Dietrich, Mol. Phys. **109**, 1169 (2011).
[22] U. Nellen, Ph.D. thesis, Physikalisches Institut der Universität Stuttgart, elib.uni-stuttgart.de/opus/volltexte/2011/6825/index.html
[23] O. V. Zvyagolskaya, Ph.D. thesis, Physikalisches Institut der Universität Stuttgart, elib.uni-stuttgart.de/opus/volltexte/2012/7347/index.html
[24] D. Bonn, J. Otwinowski, S. Sacanna, H. Guo, G. Wegdam, and P. Schall, Phys. Rev. Lett. **103**, 156101 (2009); A. Gambassi and S. Dietrich, *ibid.* **105**, 059601 (2010); D. Bonn, G. Wegdam, and P. Schall, *ibid.* **105**, 059602 (2010).
[25] O. Zvyagolskaya, A. J. Archer, and C. Bechinger, Europhys. Lett. **96**, 28005 (2011).
[26] F. Parisen Toldin, M. Tröndle, and S. Dietrich, Phys. Rev. E **88**, 052110 (2013).
[27] T. Mattos, L. Harnau, and S. Dietrich, Three-body Critical Casimir Forces, arXiv:1408.7081.
[28] M. Krech and S. Dietrich, Phys. Rev. A **46**, 1886 (1992).
[29] M. Krech and S. Dietrich, Phys. Rev. A **46**, 1922 (1992).

[30] H. W. Diehl, D. Grüneberg, and M. A. Shpot, Europhys. Lett. **75**, 241 (2006).
[31] D. Grüneberg, and H. W. Diehl, Phys. Rev. B **77**, 115409 (2008).
[32] H. W. Diehl and D. Grüneberg, Nucl. Phys. B **822**, 517 (2009).
[33] F. M. Schmidt and H. W. Diehl, Phys. Rev. Lett. **101**, 100601 (2008).
[34] H. W. Diehl and F. M. Schmidt, New J. Phys. **13**, 123025 (2011).
[35] V. Dohm, Europhys. Lett. **86**, 20001 (2009).
[36] V. Dohm, Phys. Rev. E **84**, 021108 (2011).
[37] V. Dohm, Phys. Rev. Lett. **110**, 107207 (2013).
[38] V. Dohm, Phys. Rev. E **90**, 030101(R) (2014).
[39] H. W. Diehl, D. Grüneberg, M. Hasenbusch, A. Hucht, S. B. Rutkevich, and F. M. Schmidt, Phys. Rev. E **89**, 062123 (2014).
[40] D. Danchev, Phys. Rev. E **53**, 2104 (1996).
[41] D. M. Danchev, Phys. Rev. E **58**, 1455 (1998).
[42] H. Chamati and D. M. Dantchev, Phys. Rev. E **70**, 066106 (2004).
[43] D. Dantchev, H. W. Diehl, and D. Grüneberg, Phys. Rev. E **73**, 016131 (2006).
[44] D. Dantchev and D. Grüneberg, Phys. Rev. E **79**, 041103 (2009).
[45] H. W. Diehl, D. Grüneberg, M. Hasenbusch, A. Hucht, S. B. Rutkevich, and F. M. Schmidt, Europhys. Lett. **100**, 10004 (2012).
[46] D. Dantchev, J. Bergknoff, and J. Rudnick, Phys. Rev. E **89**, 042116 (2014).
[47] R. Evans and J. Stecki, Phys. Rev. B **49**, 8842 (1994).
[48] P. Nowakowski and M. Napiórkowski, Phys. Rev. E **78**, 060602 (2008).
[49] D. B. Abraham and A. Maciołek, Phys. Rev. Lett. **105**, 055701 (2010).
[50] J. Rudnick, R. Zandi, A. Shackell, and D. Abraham, Phys. Rev. E **82**, 041118 (2010).
[51] X. Wu, N. Izmailian, and W. Guo, Phys. Rev. E **86**, 041149 (2012).
[52] D. B. Abraham and A. Maciołek, Europhys. Lett. **101**, 20006 (2013).
[53] Z. Borjan and P. J. Upton, Phys. Rev. Lett. **81**, 4911 (1998).
[54] Z. Borjan and P. J. Upton, Phys. Rev. Lett. **101**, 125702 (2008).
[55] P. J. Upton and Z. Borjan, Phys. Rev. B **88**, 155418 (2013).
[56] P. Jakubczyk and M. Napiórkowski, Phys. Rev. B **87**, 165439 (2013).
[57] A. Hucht, Phys. Rev. Lett. **99**, 185301 (2007).
[58] O. Vasilyev, A. Gambassi, A. Maciołek, and S. Dietrich, Europhys. Lett. **80**, 60009 (2007).
[59] O. Vasilyev, A. Gambassi, A. Maciołek, and S. Dietrich, Phys. Rev. E **79**, 041142 (2009).
[60] M. Hasenbusch, J. Stat. Mech.: Theor. Exp. (2009) P07031.
[61] M. Hasenbusch, Phys. Rev. B **81**, 165412 (2010).
[62] D. Dantchev and M. Krech, Phys. Rev. E **69**, 046119 (2004).
[63] M. Hasenbusch, Phys. Rev. B **82**, 104425 (2010).
[64] F. Parisen Toldin and S. Dietrich, J. Stat. Mech. (2010) P11003.
[65] M. Hasenbusch, Phys. Rev. B **83**, 134425 (2011).
[66] O. Vasilyev, A. Maciołek, and S. Dietrich, Phys. Rev. E **84**, 041605 (2011).
[67] A. Hucht, D. Grüneberg, and F. M. Schmidt, Phys. Rev. E **83**, 051101 (2011).
[68] M. Hasenbusch, Phys. Rev. B **85**, 174421 (2012).
[69] O. A. Vasilyev and S. Dietrich, Europhys. Lett. **104**, 60002 (2013).
[70] D. L. Cardozo, H. Jacquin, and P. C. W. Holdsworth, Phys. Rev. B **90**, 184413 (2014).
[71] O. A. Vasilyev, Phys. Rev. E **90**, 012138 (2014).
[72] F. Parisen Toldin, M. Tröndle, and S. Dietrich, arXiv:1409.5536.
[73] M. Hasenbusch, Phys. Rev. E **87**, 022130 (2013).
[74] J. R. Heringa and H. W. J. Blöte, Phys. Rev. E **57**, 4976 (1998).
[75] M. Caselle and M. Hasenbusch, Nucl. Phys. B **470**, 435 (1996).
[76] Y. Deng and H. W. J. Blöte, Phys. Rev. E **70**, 046111 (2004).
[77] M. Hasenbusch, Phys. Rev. B **82**, 174433 (2010).
[78] M. Campostrini, A. Pelissetto, P. Rossi, and E. Vicari, Phys. Rev. E **65**, 066127 (2002).
[79] T. W. Capehart and M. E. Fisher, Phys. Rev. B **13**, 5021 (1976).
[80] H. Hobrecht and A. Hucht, Europhys. Lett. **106**, 56005 (2014).
[81] R. C. Brower and P. Tamayo, Phys. Rev. Lett. **62**, 1087 (1989).
[82] M. Saito and M. Matsumoto, in *Monte Carlo and Quasi-Monte Carlo Methods 2006*, edited by A. Keller, S. Heinrich, and H. Niederreiter (Springer, Berlin, 2008); M. Saito, Masters thesis, Math. Dept., Graduate School of science, Hiroshima University, 2007. The source code of the program is provided at http://www.math.sci.hiroshima-u.ac.jp/~m-mat/MT/SFMT/.
[83] R. H. Swendsen and J.-S. Wang, Phys. Rev. Lett. **58**, 86 (1987).
[84] S. Todo and H. Suwa, J. Phys.: Conf. Ser. **473**, 012013 (2013).
[85] F. Gutsch, Bachelor thesis, Humboldt-Universität zu Berlin, 2014.
[86] M. Hasenbusch and S. Meyer, Phys. Rev. Lett. **66**, 530 (1991).
[87] See Supplemental Material at http://link.aps.org/supplemental/10.1103/PhysRevE.91.022110 for numerical results for $\theta_{(+,+)}$, $\theta_{(+,-)}$, $\theta_{(O,+)}$, and $\theta_{(O,O)}$.
[88] M. Hasenbusch, Phys. Rev. B **82**, 174434 (2010).
[89] B. Kaufman, Phys. Rev. **76**, 1232 (1949).
[90] B. M. McCoy and T. T. Wu, *The Two Dimensional Ising Model* (Harvard University Press, Cambridge, 1973); B. M. McCoy, in *Statistical Mechanics and Field Theory*, edited by V. V. Bazhanov and C. J. Burden (World Scientific, Singapore, 1995).
[91] J. Salas and A. D. Sokal, J. Stat. Phys. **98**, 551 (2000).
[92] M. Caselle, M. Hasenbusch, A. Pelissetto, and E. Vicari, J. Phys. A: Math. Gen. **35**, 4861 (2002).
[93] M. Hasenbusch, K. Pinn, and S. Vinti, Phys. Rev. B **59**, 11471 (1999).
[94] M. E. Fisher, *Critical Phenomena, in Proceedings of the International School of Physics Enrico Fermi, Varenna, Italy, Course LI*, edited by M. S. Green (Academic, New York, 1971).
[95] H. Kitatani, M. Ohta, and N. Ito, J. Phys. Soc. Jpn. **65**, 4050 (1996).